Materials Today Bio 19 (2023) 100611

Contents lists available at ScienceDirect

Materials Today Bio

journal homepage: www.journals.elsevier.com/materials-today-bio

Multi-modulation of immune-inflammatory response using bioactive molecule-integrated PLGA composite for spinal fusion

Hye Yeong Lee [a,1], Da-Seul Kim [b,c,1], Gwang Yong Hwang [a], Jun-Kyu Lee [b], Hye-Lan Lee [a], Ji-Won Jung [b], Sae Yeon Hwang [a,d], Seung-Woon Baek [b], Sol lip Yoon [a], Yoon Ha [a], Keung Nyun Kim [a], Inbo Han [e], Dong Keun Han [b,**], Chang Kyu Lee [a,*]

[a] Spine & Spinal Cord Institute, Department of Neurosurgery, College of Medicine, Yonsei University, Seoul, 03722, Republic of Korea
[b] Department of Biomedical Science, CHA University, Gyeonggi-do, 13488, Republic of Korea
[c] School of Integrative Engineering, Chung-Ang University, Seoul, 06974, Republic of Korea
[d] Graduate Program in Bioindustrial Engineering, Yonsei University, Seoul, 03722, Republic of Korea
[e] Department of Neurosurgery, CHA University School of Medicine, CHA Bungdang Medical Center, Gyeonggi-do, 13496, Republic of Korea

ARTICLE INFO

Keywords:
pinal fusion
PDRN
Osteogenesis
Angiogenesis
Immune-modulation

ABSTRACT

Despite current developments in bone substitute technology for spinal fusion, there is a lack of adequate materials for bone regeneration in clinical applications. Recombinant human bone morphogenetic protein-2 (rhBMP-2) is commercially available, but a severe inflammatory response is a known side effect. Bone graft substitutes that enhance osteogenesis without adverse effects are needed. We developed a bioactive molecule-laden PLGA composite with multi-modulation for bone fusion. This bioresorbable composite scaffold was considered for bone tissue engineering. Among the main components, magnesium hydroxide (MH) aids in reduction of acute inflammation affecting disruption of new bone formation. Decellularized bone extracellular matrix (bECM) and demineralized bone matrix (DBM) composites were used for osteoconductive and osteoinductive activities. A bioactive molecule, polydeoxyribonucleotide (PDRN, PN), derived from trout was used for angiogenesis during bone regeneration. A nano-emulsion method that included Span 80 was used to fabricate bioactive PLGA-MH-bECM/DBM-PDRN (PME2/PN) composite to obtain a highly effective and safe scaffold. The synergistic effect provided by PME2/PN improved not only osteogenic and angiogenic gene expression for bone fusion but also improved immunosuppression and polarization of macrophages that were important for bone tissue repair, using a rat model of posterolateral spinal fusion (PLF). It thus had sufficient biocompatibility and bioactivity for spinal fusion.

1. Introduction

Spinal fusion is a fundamental surgical technique used to restore spinal instability for degenerative diseases, trauma and deformities, tumors, and infections [1–3]. Pseudoarthrosis (failure of spinal fusion) is a serious and challenging complication of spinal fusion surgery, which leads to severe pain and mobility impairment [4]. Due to osteoporosis, most elderly patients who require spinal fusion have fragile bones [2,5,6]. Although it is important that a functional spinal unit maintains the biomechanical spinal properties of the entire spine [7], spine fusion healing requires a long period; long-term fixation of the spine for fusion after surgery can also cause systemic complications [8,9]. Various materials have been examined as autogenous bone substitutes to enhance spinal fusion rates (e.g., allogeneic bone graft material (DBM), synthetic bone graft materials (tricalcium phosphate, hydroxyapatite, and bioglass), and bone morphogenetic protein-2 (BMP-2)). Recombinant human BMP-2 (rhBMP-2) is commercially available, has US Food and Drug Administration approval, and is widely used in spinal fusion surgery due to the high potency of the fusion process. However, use of this product can lead to serious complications, such as heterotopic

* Corresponding author.
** Corresponding author.
E-mail addresses: dkhan@cha.ac.kr (D.K. Han), NSCKLEE@yuhs.ac (C.K. Lee).
[1] These authors contributed equally to this work.

https://doi.org/10.1016/j.mtbio.2023.100611
Received 20 January 2023; Received in revised form 3 March 2023; Accepted 11 March 2023
Available online 14 March 2023

ossification and soft tissue inflammation [10,11]. Therefore, researchers and clinicians have worked to develop efficient and safe non-stationary materials.

To encourage tissue regeneration by mimicking the natural microenvironment, bone tissue engineering studies have focused on the functionalized artificial scaffold containing extracellular matrix (ECM) [12]. These scaffolds provide better cell adhesion, migration, proliferation, and differentiation [13–15]. Bone fusion engineering has the ultimate goal of regenerating damaged or lost bone tissue via osteoconductive and/or osteoinductive scaffolds [16]. The synthesized scaffold modulates the host bone microenvironment for better adhesion, growth, and differentiation of stem cells, which results in better new bone and fusion [17]. With the design of an artificial bone tissue engineering scaffold, the synthesized scaffold containing ECM could accelerate bone fusion. Although hydroxyapatite (HA) and β-tricalcium phosphate (β-TCP) are used for osteoconductivity of the scaffold, there are differences in calcium and phosphate ratios (1.72 and 1.5, respectively), compared with natural bone (1.67). However, because decellularized bone ECM (bECM, inorganic ECM) has the same Ca/P ratio as that of real bone, it can support effective bone regeneration and has great osteoconductive ability [18–20]. Demineralized bone matrix (DBM, organic ECM) is widely used in spinal fusion surgery and consists of active organic components such as collagen and glycoproteins [10,21]. In this study, we were inspired by an inorganic-organic composition (7:3) of natural bECM. Our hypothesis was that the natural bone mimetic scaffold would have outstanding new bone formation and bone fusion performance.

There have been various attempts to functionalize the synthetic scaffold using bioactive molecules for bone tissue engineering. We found that polydeoxyribonucleotide (PDRN, PN) has an excellent effect on angiogenesis during bone regeneration [20]. PDRN is a short bioactive DNA molecule (50–200 base pairs) from trout (*Oncorhynchus mykiss*) gonads; it acts as an adenosine A2a receptor agonist [22]. Adenosine A2a receptors are G-protein-coupled transmembrane receptors. They occur in numerous cells, including immune cells, endothelial cells, and epithelial cells. Adenosine and its agonist have therapeutic effects such as wound healing, angiogenesis, anti-inflammation, and immunosuppression. Cekic et al. found that the adenosine A2a receptor facilitates immunosuppression with M2 macrophage polarization [23].

Bioresorbable scaffolds are a promising tool for spinal fusion. Among them, poly(lactic-co-glycolic acid) (PLGA) is a popular biopolymer for bone implants due to its biodegradability and low cytotoxicity. The hydrolyzed PLGA degradation product, lactic acid and glycolic acid, can induce local inflammation at the implant site [24,25]. Acute inflammation can aggravate non-union and disrupt new bone formation after spinal fusion surgery. Hence, we found that use of magnesium hydroxide (MH)-incorporated PLGA composite effectively alleviates inflammation via reduction in local pH conditions [10]. However, PDRN is water-soluble and can aggregate in organic solvents. Therefore, to fabricate homogeneous dispersion in hydrophobic PLGA composite, we adopted a nano-emulsion-based dispersion method using Span 80 [26].

2. Material and methods

2.1. Homogenous dispersion, PLGA composite fabrication, and characterization

Poly(lactic-co-glycolic acid) (PLGA; lactide:glycolide = 50:50, Resomer RG505) was purchased from Evonik Ind. (Essen, Germany). Magnesium hydroxide (MH, 632,309) was purchased from Sigma-Aldrich (MO, USA). All composites (PLGA, PM, PME2, and PME2/PN) were prepared using a solvent casting method. Before blending, the MH was ground using a 6775 Freezer/Mill® Cryogenic Grinder (SPEX SamplePrep, NJ, USA). As a phase emulsifier, 333 μL Span® 80 (85,548, Sigma-Aldrich) was added to 10 mL chloroform. Subsequently, 2 g PLGA, 400 mg cryomilled-MH powder, 600 mg bovine-derived decellularized ECM (bECM and inorganic ECM; Oscotec Inc., Seongnam, Korea), 257 mg DBM (DBM, organic ECM; Hans Biomed Co., Seoul, Korea), and 400 mg PDRN (GoldBio, St. Louis, MO, USA) were mixed with 10 mL chloroform/Span® 80 solution. The dispersed solution was poured into a Teflon mold (30 × 90 mm, rectangular shape) and the solvent was drawn off to leave a polymer film adhering to the mold overnight. After all solvent evaporated, the film was carefully detached from the mold and bioinspired PLGA composites were obtained.

Morphological surface images of the composites were obtained using field emission-scanning electron microscopy (FE-SEM; SIGMA, Carl Zeiss, Germany). PDRN dispersion on the composite was visualized using fluorescence microscopy (DP-74, Olympus, Tokyo, Japan) after staining with Hoechst 34,580 (H21486, Invitrogen, Thermo Fisher Scientific, Waltham, MA, USA). Degradation properties of the composites (12 × 4 × 0.1 mm) were performed in 1 mL PBS solution at 37 °C for 70 days. PDRN release profiles were measured using a NanoDrop One/One^{c} (Thermo Fisher Scientific).

2.2. Cell cytotoxicity and proliferation analysis

Human bone marrow-derived mesenchymal stem cells (hBMSCs) were purchased from Lonza (PT-2501, Basel, Switzerland). hBMSCs were expanded with Dulbecco's modified Eagle's medium (DMEM)/low glucose medium (HyClone, Cytiva, MA, USA) supplemented with 10% fetal bovine serum (FBS) (Gibco, Thermo Fisher Scientific), and antibiotic/antimycotic solution (100X) (LS 203–01, WELGENE, Korea). hBMSCs were grown at 37 °C in a humidified 5% CO_2 atmosphere. The medium was changed every 2–3 days.

Live and dead staining were performed using calcein AM (C3099, Invitrogen, Thermo Fisher Scientific) and ethidium homodimer-1 (EthD-1, E1169, Invitrogen, Thermo Fisher Scientific). Cell proliferation assay was performed using a D-Plus™ cell counting kit 8 (CCK-8, Dongin LS, Korea) at 1, 3, and 7 days. Colorimetric measurement results were read at a wavelength of 450 nm using a microplate reader (SpectraMax M2, Molecular Devices, CA, USA).

2.3. In vitro RNA extraction and quantitative real-time PCR

hBMSCs were indirectly cultured using cell culture inserts (36,224, SPL, Korea). RNA was extracted using a Universal RNA Extraction Kit (K-3141, Bioneer, Korea), following the manufacturer's instructions. Extracted RNA was reverse-transcribed to complementary DNA using a PrimeScript RT Reagent Kit (Perfect Real Time, Takara, Tokyo, Japan). qRT-PCR was performed using each primer and SYBR Green PCR Master Mix (Applied Biosystems, Thermo Fisher Scientific). Expression of proinflammation-, angiogenesis-, and osteogenesis-related genes were calculated with 18S ribosomal RNA as a reference and using the $2^{-\Delta\Delta Ct}$ method.

2.4. Macrophage polarization

RAW264.7 cells, a murine macrophage cell line, were obtained from the Korean Cell Line Bank (KCLB, Seoul, Korea) and cultured in DMEM/high glucose medium (HyClone) supplemented with 10% FBS and 1% antibiotic/antimycotic solution (100X). RAW264.7 cells were seeded into a 24-well plate at a density of 5 × 10^4 cells per well and were stimulated with 50 ng/mL IFN-γ (R&D systems) and 10 ng/mL lipopolysaccharide (Sigma-Aldrich), followed by co-culture with the composites, using cell culture inserts for 24 h.

2.5. Immunocytochemistry

hBMSCs, RAW264.7 cells, and human umbilical vein endothelial cells (HUVECs) were fixed in 4% paraformaldehyde solution for 15 min. Fixed cells were washed carefully with a PBS solution three times and were then permeabilized for 15 min with 0.3% Triton X-100 in PBS solution. To reduce the nonspecific background, the cells were blocked with a 5%

BSA in PBS solution for 1 h. After blocking, the cells were incubated with primary antibodies overnight at 4 °C. The cells were subsequently rinsed with PBS solution and incubated with secondary antibodies for 1 h at RT. After antibody labeling, cells were washed with PBS solution, and nuclei were stained with Hoechst 34,580. The primary antibodies included anti–NF–κB (1:200; sc-8414, Santa Cruz Biotechnology, CA, USA), anti-Arginase 1 (1:200; sc-271,430, Santa Cruz Biotechnology), and anti-iNOS (1:500; Invitrogen, Thermo Fisher Scientific). The secondary antibodies included Alexa Fluor™ 488 donkey anti-rabbit IgG (H + L) and Alexa Fluor™ 555 donkey anti-mouse IgG (H + L) (A-21206 and A-21422, Invitrogen, Thermo Fisher Scientific).

2.6. Wound healing assay and tubule formation

A scratch assay and tubule-forming assay were performed on HUVECs. Briefly, HUVECs were seeded at a density 5×10^5 cells/well in 6-well plates for 24 h. The cell layers were then scratched to form wound gaps. The cells were treated with conditioned media for 18 h, images were visualized at 0 and 18 h. To assess tubule-forming ability, HUVECs were seeded in a 24-well plate coated with Matrigel (356,234; Corning, NY, USA), and treated with conditioned media. After incubation at 37 °C and 5% CO_2 for 18 h, the cells were stained with 2 μg/mL calcein AM. The number of branch points and total tube lengths were measured using the ImageJ angiogenesis plug-in (NIH, MD, USA).

2.7. Osteogenic differentiation

To analyze osteogenic ability of the composites, hBMSCs were seeded in 24-well plates (5×10^4 cells/well). After 1 day, the medium was replaced with an osteogenic induction medium containing 10% FBS, 1% antibiotic/antimycotic solution (100X), 50 μM L-ascorbic acid, 0.1 μM dexamethasone, and 10 mM β-glycerophosphate. ALP staining was performed using an ALP staining kit (MK300, Takara, Japan) at 7 days after osteogenic induction. Subsequently, ALP activity was quantified using an ALP assay kit (MK301, Takara). After 21 days of osteogenic induction, mineralized ECM was stained with Alizarin Red S (A5533; Sigma-Aldrich). The cells were fixed with 10% formalin for 15 min and washed with deionized water. Each plate was incubated in 2% Alizarin Red S solution for 20 min at 25 °C. Stained cells were examined using an optical microscope. To quantify the staining results, 10% cetylpyridinium chloride (CPC; C0732, Sigma-Aldrich) solution was added to each well and incubated for 15 min to elute at 25 °C. Colorimetric measurement results were read at a wavelength of 562 nm using a microplate reader.

2.8. Posterolateral lumbar fusion model and surgical procedure

In this study, we used 115 male Sprague Dawley rats (250 ± 15g, mean ± standard deviation; OrientBio, Kyungki-do, Korea) with 20–25 rats in 5 groups. The rats were housed in an animal facility permitted by the Association for Assessment and Accreditation of Laboratory Animal Care. Each rat was anesthetized using ketamine (100 mg/kg; Yuhan, Seoul, Korea), Rompun (10 mg/kg; Bayer, Leverkusen, Germany), and isotroy 100 (Troikaa Pharmaceuticals Ltd, Gujarat, India). After aseptically preparing the lumbar region, the muscle was cut to expose a section from the transverse processes to the neural arch region at L4-L5. The neural arch surface was decorticated using a scalpel and a low-speed drill bilaterally. The scaffold (12 × 4 × 0.1 mm) was transplanted to the exposed neural arch site, and the autologous iliac bone chip 200 mg was transplanted bilaterally (Fig. 1A and B). The experimental groups were managed using the following methods: 1. Auto bone graft, Ctrl; 2. ABG + PLGA, PLGA; 3. ABG + PLGA/magnesium hydroxide, PM; 4. ABG + PM/ECM: DBM, PME2; 5. ABG + PME/PDRN, PN: sorbitan monooleate, PME2/PN.

All experimental procedures were performed according to protocols approved by the directives of the Institutional Animal Care and Use Committee (IACUC; Protocol number: 2021–0202).

2.9. Microcomputerized tomography analysis for new bone formation

The rats were sacrificed at 8 weeks postoperatively, and the lumbar spines were harvested immediately from the 1st lumbar to the 1st sacral vertebrae. The obtained spine samples were fixed using 10% formalin at 25 °C for 7 days for micro-computerized tomography scanning to measure the calcified fusion mass at the region of PLF. Each spine sample was scanned in a SkyScan 1173 micro-CT imager (Bruker-CT, Kartuizersweg 3B 2550 Kontich, Belgium) and was analyzed using image controlling software (version 1.6, SkyScan 1173, Bruker-CT, Kontich, Belgium). Each scan was performed in the long axis of the spine with an energy of 130 kVp and a current of 60 μA; a resolution of 25 μm voxel size was used and 800 slices were taken. An aluminum filter of 1.0-mm thickness was used to increase the mean photon energy of the source X-ray beam. Raw image data were 3D reconstructed using CTVOX (Ver. 3.3.0, Bruker-CT, Kartuizersweg 3B 2550 Kontich, Belgium). Reconstructed images of scanned spine samples were analyzed using CTAn Software (Ver. 1.19.40., Bruker-CT, Kartuizersweg 3B 2550 Kontich, Belgium). The implant materials and bone tissue were analyzed separately.

2.10. Biomechanical bending tests

After 8 weeks, we surgically removed three segments out of the test subjects, including the fused mass. All harvested PLF masses were evaluated using a three-point bending test and Universal Testing Machine (TO-101, Testone, Seoul, Korea). Both ends of the vertebral bodies were placed with their dorsal sides down on two fulcra. The upper anvil (10.0-mm diameter) was placed in a position to apply a load to the ventral surface of the intervertebral disc, perpendicular to the longitudinal spine. Three-point bending tests were performed with a 10.0-mm intersupport distance and a 50-mm/min crosshead speed until the upper anvil was advanced to 15 mm. The curve force-displacement results from these tests indicated flexural strength based on bending point and modulus based on slope.

2.11. Histological assessment

2.11.1. Sample preparation

For histological analysis, the bone samples were fixed in 10% formalin and were dehydrated with ascending ethanol concentrations. Ultraviolet light-activated polymethylmethacrylate (Technovit 7200, VLC, Kulzer GmbH Division Technik Philipp-Reis-Str. 8/13 61,273 Wehrheim, Germany) was used as an infiltration medium. After penetration of the whole specimen with the embedding medium, high power UV-light sources were used during the last stage of polymerization to ensure that the medium was fully hardened (Exakt 520, EXAKT Advanced Technologies GmbH Robert-Koch-Str. 522,851 Norderstedt). Parallel sections of 300–400 μm thickness were then cut from the specimen using a micro-sawing machine (EXAKT 300, EXAKT Advanced Technologies). The desired final thickness of the specimen (40–70 μm) needed for special staining and light microscopic analysis was obtained using a micro-grinding system (EXAKT 400 CS, EXAKT Advanced Technologies) and sandpaper.

2.11.2. Hematoxylin and eosin staining

Each section was stained using an ordinary H&E staining method. First, each section, including nuclei, was stained using hematoxylin (Dako, Glostrup, Denmark) at 37 °C for 10 min and then washed. The tissue was then differentiated in 0.35% acid alcohol solution and treated with bluing solution that was 1% lithium carbonate. The tissue was then washed again. Cytosol staining using 1% alcoholic Eosin Y solution for 5 min, and a wash, were used for the next step. Finally, the sections were dehydrated using graded ethanol (70–100%) and were then mounted (Permount™ Mounting Medium, Electron Microscopy Science). The samples were examined under a Digital slide scanner (PANNORAMIC 250 Flash III, 3DHISTECH Ltd. H-1141 Budapest, Öv u. 3., Hungary).

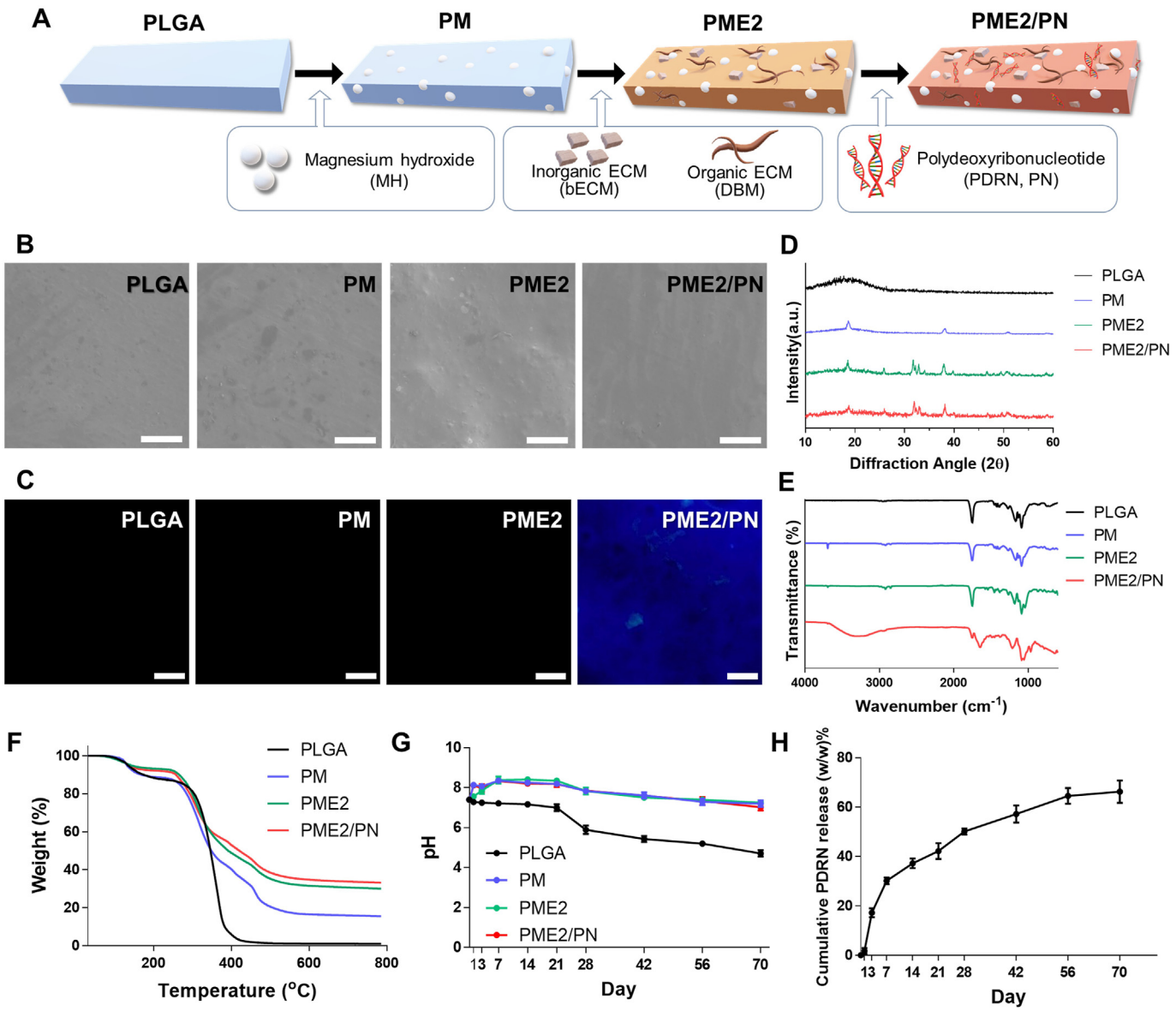

Fig. 1. Fabrication of homogenous dispersed PME2/PN composite using a nano-emulsion method with Span 80. (A) Schematic illustration of PLGA, PM, PME, and PME2/PN composites preparation. (B) Representative SEM images of each composite. Scale bars, 200 μm. (C) Fluorescent microscopy images of composites stained with Hoechst stain. Scale bars, 100 μm. (D) Diffraction pattern observed from X-ray diffraction (XRD). (E) Attenuated total reflectance-Fourier transform-infrared spectroscopy (ATR-FTIR) spectra of the composites. (F) Thermogravimetric analysis (TGA) thermograms for each composite (100–800 °C). (G) pH changes of composites during *in vitro* degradation in PBS solution at 37 °C. (H) PDRN release profile from PME2/PN *in vitro*.

2.11.3. Goldner's trichrome staining

Samples were stained using Weiger's hematoxylin (Thermo Fisher Scientific) for 5 min. They were then washed in tap water, stained in ponceau acid fuchsine for 5 min, washed in 1% acetic acid, and placed in phosphomolybdic acid orange G solution (Sigma) until the collagen was decolorized. The samples were then rinsed in 1% acetic acid, stained in a light green stock solution for 10 min, and rinsed again in 1% acetic acid. Finally, the slides were dehydrated using graded ethanol and mounting medium.

2.11.4. von Kossa staining

Samples were exposed to strong light until the mineralized bone turned black with 1% silver solution for 30–60 min. Then, the slides were rinsed with distilled water and quickly dipped into 5% sodium thiosulfate before staining with Nuclear Fast Red Solution (Sigma) for 5 min. After dehydration, the sections were mounted with permount medium.

2.12. Gene and protein analysis

2.12.1. Sample preparation and RNA extraction

Extracts of the lumbar 4–5 region of rats were taken, without the surrounding soft tissue. These samples were flash frozen using liquid nitrogen and were crushed to a fine powder using a liquid nitrogen-cooled mortar.

2.12.2. qRT-PCR

The total RNA from sample tissue and scaffolds was isolated using TRIzol reagent (Thermo Fisher Scientific), following the manufacturer's instructions. The RNA pellet was resuspended, and the RNA concentration was determined. The RNA was reverse-transcribed using amfiRivert cDNA Synthesis Platinum Master Mix (GenDEPOT, Barker, TX) in duplicate for each sample. PCR was performed using Power SYBR® Green PCR Master Mix (Thermo Fisher Scientific) with a QuantStudio 3

real-time PCR instrument (Applied Biosystems). The PCR conditions were: 95 °C for 10 min and 40 cycles of 95 °C for 15 s, 60 °C for 60 s, and 72 °C for 30 s. The relative osteogenic, angiogenic, and inflammatory gene levels were calculated using GAPDH as a reference gene.

2.12.3. Western blot analysis

Sample tissues were lysed in standard radioimmunoprecipitation assay buffer (Thermo Fisher Scientific) containing Halt protease inhibitor Single-Use Cocktail (Thermo Fisher Scientific) on ice for 30 min. Protein was quantified using a Pierce™ BCA Protein Assay Kit (Thermo Fisher Scientific). Proteins (20 μg) were separated using polyacrylamide gel electrophoresis and 10% gels and were transferred to polyvinylidene difluoride membranes. The membranes were blocked in TBS plus 5% non-fat milk powder and 0.1% Tween 20 for 1 h before incubating with the following antibodies overnight at 4 °C: anti-osteocalcin, fibromodulin, VEGF-A, and GAPDH (Abcam). Antigen–antibody complexes were detected using secondary antibodies conjugated to horseradish peroxidase (HRP). They were visualized using enhanced chemiluminescence (GE Healthcare, Piscataway, NJ, USA). Quantitation of band intensity was performed using Image J software.

2.13. Statistical analysis

All results were presented as mean ± standard error except standard deviation values, in qPCR results. All experimental data were analyzed using ordinary one-way ANOVA with Tukey's multiple comparisons tests. GraphPad Prism 9.41 for Windows (GraphPad Software, USA) was used for these analyses.

3. Results

3.1. Fabrication of bioinspired homogeneous dispersion PLGA composite

The PLGA was a pivotal matrix of composites prepared using a previously reported solvent casting method [27] (Fig. 1A). To fabricate homogeneously PDRN-dispersed PLGA composite, Span 80 (a water in oil emulsifier) was used to form a nano-emulsion in organic solvent [26]. Surface morphological properties were investigated using scanning electron microscopy. Comparing the images of the PME2/PN with and without Span 80 revealed that the surface roughness was significantly increased with no Span 80 present, suggesting that the PDRN without Span 80 formed aggregation due to low dispersibility in the composite (Fig. 1B and Supplementary Fig. 1). Similarly, DNA specific staining (Hoechst) revealed homogenous PDRN distribution in the PME2/PN treatment with Span 80. Addition of functional molecules, including MH, bECM, DBM, and PDRN in the PLGA composite resulted in improvement (Fig. 1C). X-ray diffraction (XRD) was executed to examine whether composite's crystalline structure was changed (Fig. 1D). In XRD spectra, the all groups except PLGA showed $Mg(OH)_2$ peaks at 2θ value of 18.105°, 38.445°, and 51.255° corresponding to (001), (011), and (012) planes, respectively, and the PME2 and PME2/PN exhibited calcium and phosphorous peaks.

The surface composition of the composites was confirmed using ATR-FTIR (Fig. 1E). The P–O and C–O stretches and PO^{2-} symmetric stretches (1071 and 1097 cm^{-1}) by the phosphodiester backbone of DNA were displayed in FTIR spectra.

The proportions of MH, dECM, and DBM in the composites were determined using thermogravimetric analysis (Fig. 1F). The water contact angles for PLGA, PM, PME2, and PME2/PN were 87.33°, 75.98°, 58.23°, and 53.02°, respectively (Table S1). Degradation behavior is one of the most challenging characteristics of biomaterial design. PLGA degradation byproducts can occur after implantation in an acidic microenvironment. Therefore, we incorporated magnesium hydroxide, which has an excellent pH neutralization effect [28–30]. To assess pH-dependent degradation behavior, the composites were immersed in phosphate-buffered saline (PBS) solution at 37 °C for 70 days. While in PBS solution, the pH of the PLGA composites declined to 4.7. However, in the groups containing MH, the pH was maintained at up to 7.0 (Fig. 1G). The PDRN release profile was investigated at 260 nm, a double-strand DNA quantifiable UV absorbance (Fig. 1H). PDRN was sustainably released from the PME2/PN during the 70-day period.

3.2. Anti-inflammation and immune-modulating effects of PME2/PN

To investigate biocompatibility of PME2/PN, live/dead staining was performed using human bone marrow mesenchymal stem cells (hBMSCs). Due to the well-known biocompatibility of PLGA, the population of live cells (calcein AM-stained cells) was larger than that of the EthD-1 (ethidium homodimer-1)-positive cells that indicated the presence of dead cells (Fig. 2A). However, calcein AM-positive cell populations were gradually increased in the PM, PME2, and PME2/PN groups. Cell viability was revealed at 1 and 3 days *in vitro* using CCK-8 analysis (Fig. 2B). Due to better hydrophilicity, initial cell proliferation at 1 day in the PME2/PN group was greater than in the other groups. The anti-inflammation response of the PME2/PN was assessed using expression of pro-inflammatory cytokine-related genes, including tumor necrosis factor-α (TNF-α), interleukin-6 (IL-6), and Interleukin-1β (IL-1β); qRT-PCR analysis of the composites was performed after a 3-day culture (Fig. 2C).

The TNF-α mRNA had significantly lower expression in the PM ($p < 0.05$), PME2 ($p < 0.05$), and PME2/PN ($p < 0.01$) groups than in the PLGA groups. The same mRNA expression patterns were observed in the IL-6 and IL-1β groups. To clarify the anti-inflammation ability of PME2/PN, nuclear translocation of NF-κB was investigated using immunocytochemistry (ICC) with anti–NF–κB antibody (Fig. 2D). The groups containing MH attenuated translocation of NF-κB more than in the PLGA group. The PDRN-incorporated composite had the most effective attenuation of NF-κB translocation in the hBMSCs.

Macrophage phenotypic transition ability was examined using M1-induced murine-derived macrophage cells (Raw 264.7), interferon-γ (IFN-γ), and lipopolysaccharide (Fig. 2E). After M1 induction, expression of inducible nitric oxide synthase (iNOS), an M1 macrophage-specific marker, increased in the control and PLGA groups. Despite the PM and PME2 groups having reduced populations of iNOS-positive cells and increased numbers of arginase 1 (Arg1)-positive cells, the PME2/PN had even greater effects regarding M1-to-M2 polarization of macrophages. Taken together, these results indicated that PME2/PN promoted biocompatibility and bioactivity for spinal fusion.

3.3. Angiogenic and osteogenic capabilities of PME2/PN in vitro

Studies have highlighted the angiogenic effect of PDRN [31,32]. Angiogenesis has an important role in fracture healing and repair [33] and, consequently, has cell signaling pathways that are coupled with osteogenesis. Wound healing and tube formation analysis was performed to examine the pro-angiogenic ability of the PME2/PN using human umbilical vein endothelial cells (HUVECs) cultured in conditioned medium immersed the composites for 24 h (Fig. 3A and B). Wound areas gradually decreased in different patterns in the PM, PME2, and PME2/PN groups. The tubule-forming assay revealed that the number of branch points and total tube lengths substantially increased in the PDRN-containing group. Angiogenesis-related gene expression was evaluated using qRT-PCR (Fig. 3C). VEGF-A, a major regulator of angiogenesis, is secreted by osteoblasts and hypertrophic chondrocytes and can be involved in osteoblast differentiation [33]. Ang1 is expressed in endothelial cells and has important roles in vascular growth, remodeling, and maturation. It is a strong anti-apoptotic factor in mesenchymal stem cells and an important factor with many effects on osteoblast differentiation and bone formation [34].

In the PME2/PN group, the VEGF-A gene expression was 2.21-fold higher than in the PLGA group. of In the PME2/PN group, hepatocyte growth factor (HGF), platelet-derived growth factor (PDGF), fibroblast

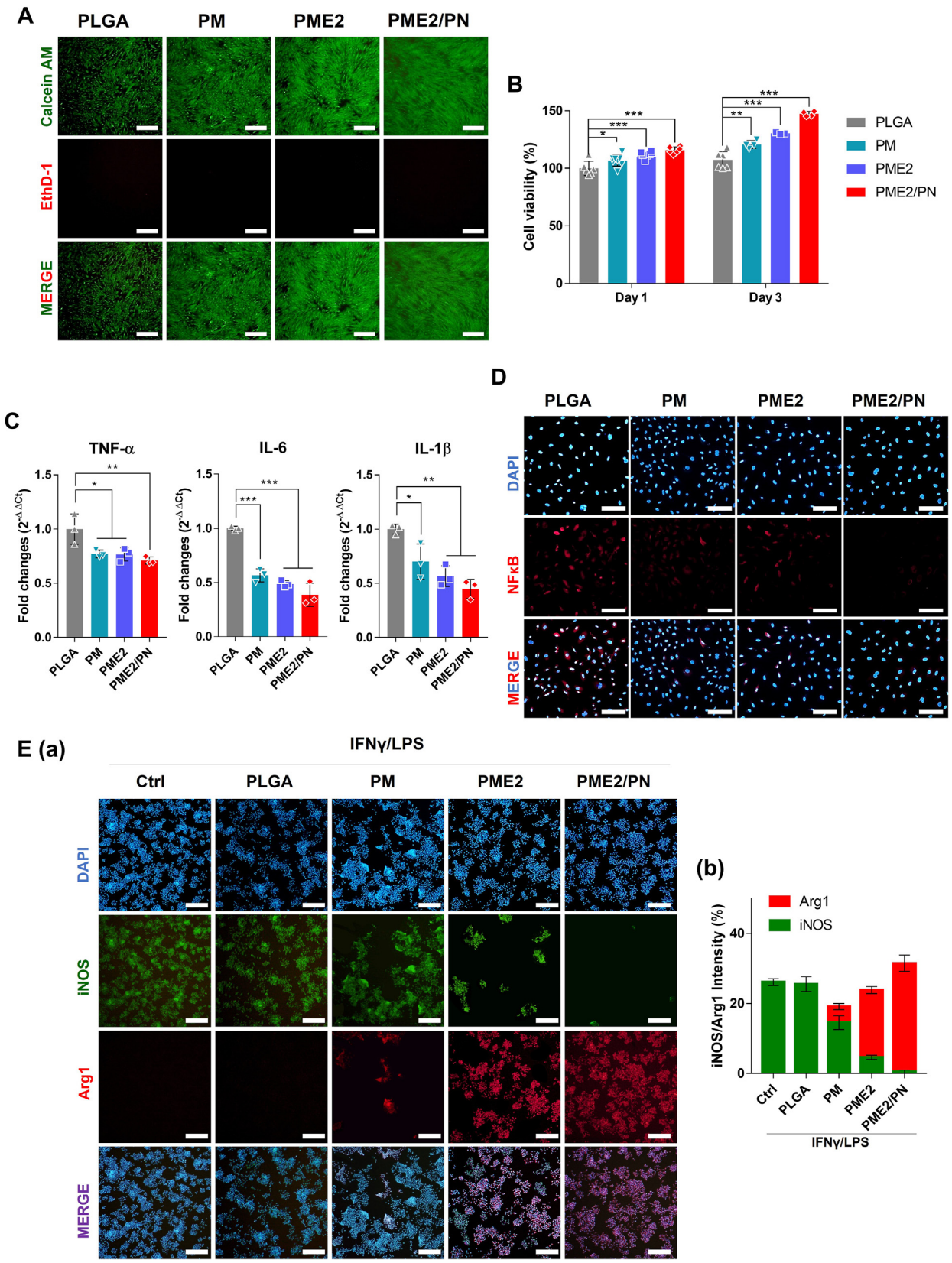

Fig. 2. Multi-modulation of immune-inflammatory response of PME2/PN composite. (A) Cell cytotoxicity investigation using live/dead staining images of hBMSCs after a 24-h treatment. Scale bars, 500 μm. (B) hBMSC viability on each composite at 1 and 3 days *in vitro*. (C) Pro-inflammatory marker expression, including TNF-α, IL-6, and IL-1β in hBMSCs, qRT-PCR analysis. (D) Representative ICC staining images using HUVECs labeled with anti–NF–κB antibody. Scale bars, 100 μm. (E) ICC staining images and corresponding quantification of iNOS (green), CD206 (red), and nuclei (blue) of murine macrophage cells (RAW264.7) after M1 induction. Scale bars, 200 μm $^{*}p < 0.05$, $^{**}p < 0.01$, and $^{***}p < 0.001$ indicate statistically significant differences.

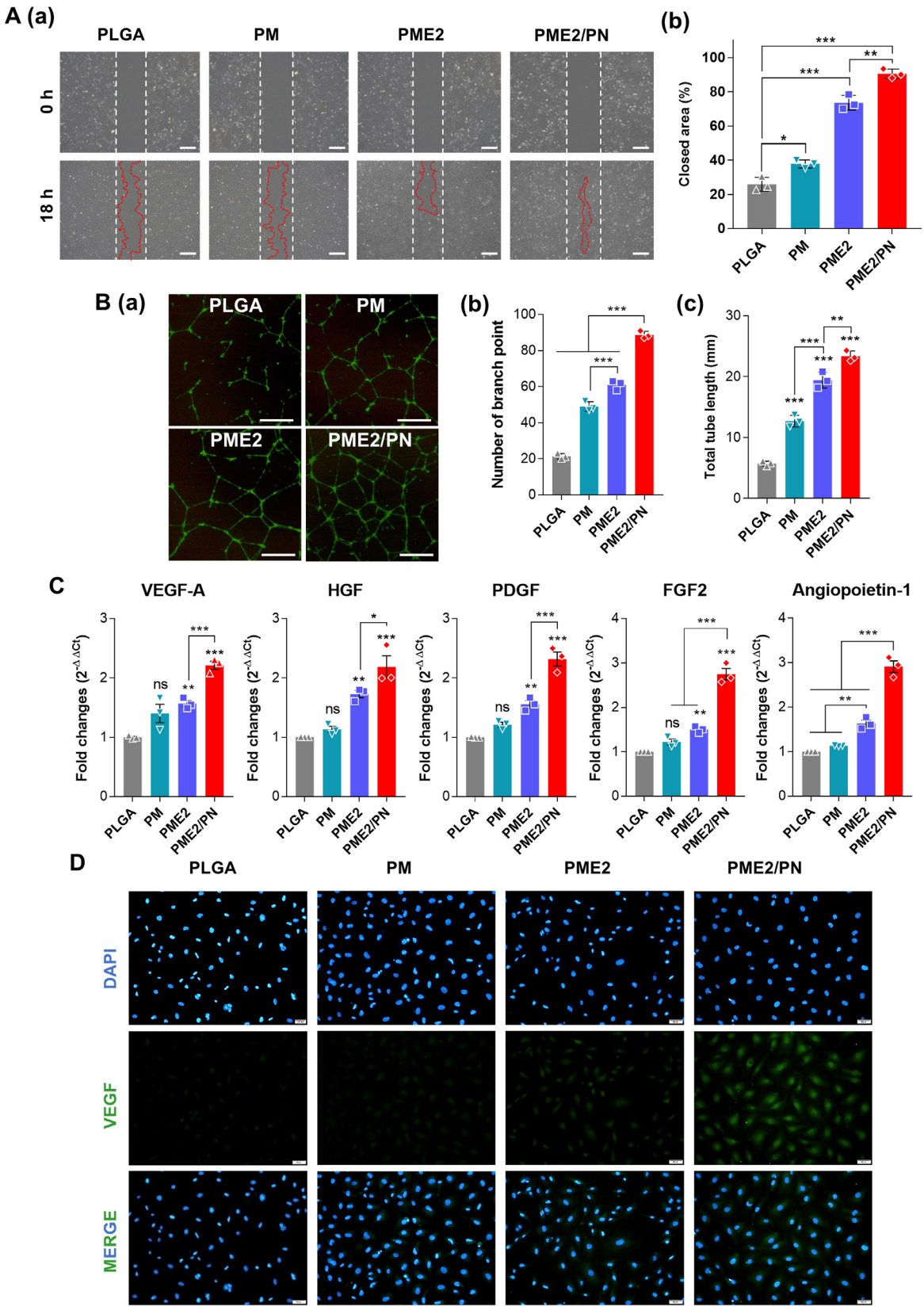

Fig. 3. Angiogenic ability of PME2/PN *in vitro*. (A) Cell migration assay images and quantification using HUVECs, at 18 h. Scale bars, 500 μm. (B) Tubule forming assay images and quantification using HUVECs stained with calcein AM. (C) Expression of angiogenesis markers, including VEGF-A, HGF, PDGF, FGF2, and angiopoietin-1 (Ang1) in HUVECs, qRT-PCR analysis. (D) Representative ICC staining images using HUVECs labeled with anti-VEGF antibody. Scale bars, 100 μm $^{*}p < 0.05$, $^{**}p < 0.01$, and $^{***}p < 0.001$ indicate statistically significant differences.

growth factor-2 (FGF2), and angiopoietin-1 (Ang1) genes were expressed more than 2-fold higher than in the PLGA group. To investigate VEGF protein production, ICC staining was performed using anti-VEGF antibody (Fig. 3D). Like the qPCR result, the group containing PDRN had enhancement of the population of VEGF-positive cells.

To examine osteogenic efficacy, hBMSCs were cultured in osteogenesis induction medium. Alkaline phosphatase (ALP) staining and activity quantification were performed after 7 days of differentiation. Representative stained images revealed that the PME2/PN group had higher ALP expression (Fig. 4A). Quantified ALP activity was enhanced by 120.62%, 157.23%, and 202.82% in the PM, PME2, and PME2/PN groups, compared with the PLGA. Furthermore, the effect on mineralization was investigated after 21 days of differentiation using Alizarin Red S staining and calcium elution assay (Fig. 4B). In Fig. 4B (b), the PME2/PN group had a significantly increased calcium deposition rate, compared with the PLGA, PM, and PME2 groups. A genetic assessment was performed using a variety of osteogenesis-related gene expressions, including ALP, runt-related transcription factor 2 (RUNX2), fibromodulin (FMOD), osteocalcin, and osteopontin; the qRT-PCR analyses were performed at 21 days after osteoinduction (Fig. 4C). ALP is a crucial regulator enzyme in bone mineralization [35]. It provides inorganic phosphate from pyrophosphate and phosphomonoesters and hydrolyzes pyrophosphate, mineralization inhibitor, for the hydroxyapatite synthesis. RUNX2, a critical transcription factor for osteoblastogenesis, has peak expression in immature osteoblasts; expression decreases in mature osteoblasts [36]. FMOD is expressed in both chondrocytes and osteoblasts

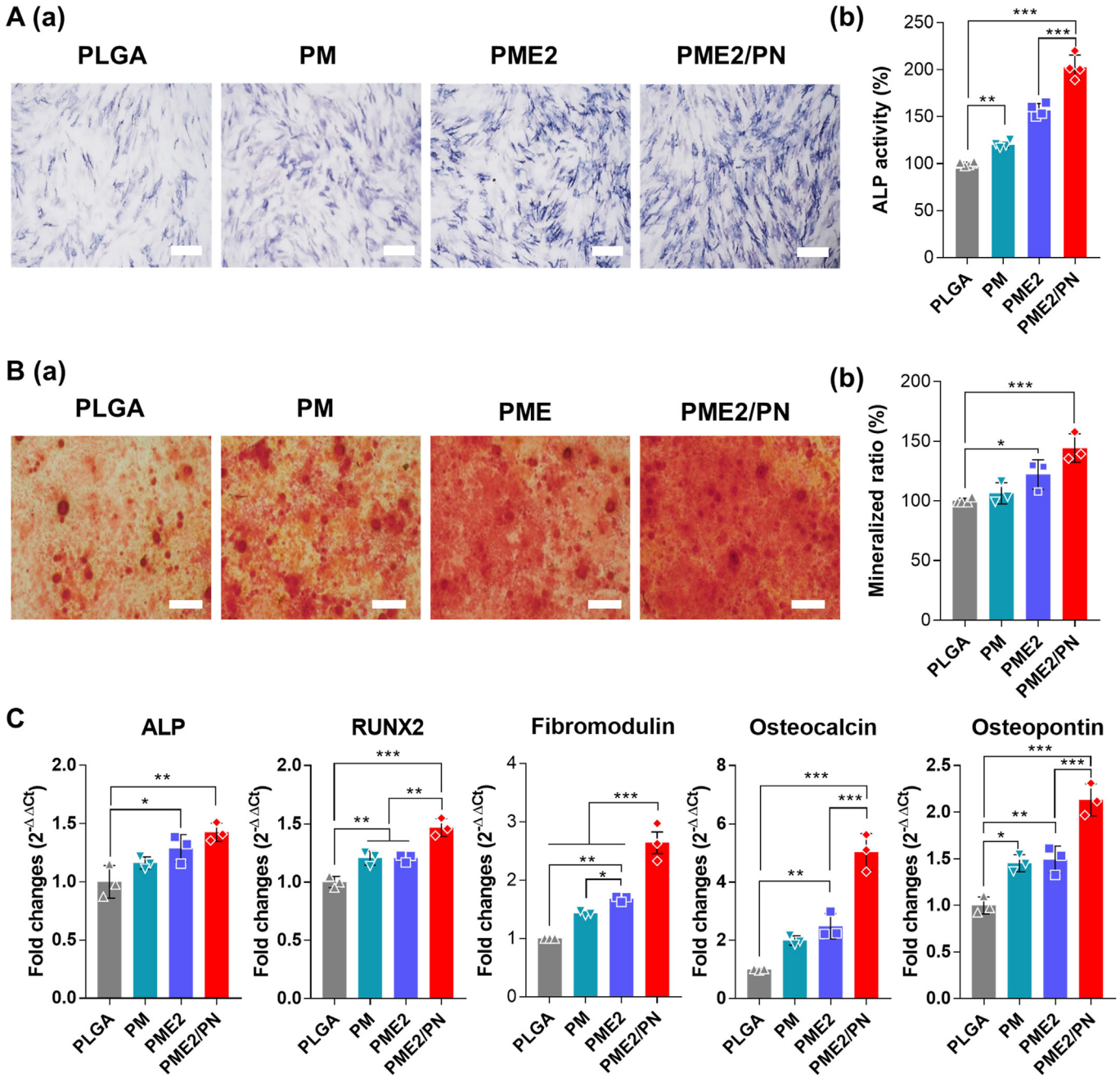

Fig. 4. Osteogenic ability of PME2/PN *in vitro*. (A) ALP-stained images and ALP activity quantification. Scale bars, 500 μm. (B) Alizarin Red S staining images (a) and calcium deposition quantification (b). Scale bars, 500 μm. (C) Expression of osteogenic markers, including ALP, RUNX2, fibromodulin (FMOD), osteocalcin, and osteopontin in hBMSCs, qRT-PCR analysis. $^{*}p < 0.05$, $^{**}p < 0.01$, and $^{***}p < 0.001$ indicate statistically significant differences.

during early development, but transcriptional expression is lost in maturation and in aggregated cartilage [37]. FMOD is a collagen-binding glycoprotein; it affects mineralization while supporting apatite formation [38]. Bone γ-carboxyglutamic acid-containing protein (i.e., osteocalcin) is the most abundant noncollagenous matrix protein expressed in osteoblasts [39]. As a result, γ-carboxyglutamic acid residues of osteocalcin bind calcium and hydroxyapatite, which results in accumulation of osteocalcin in the mineralized matrix [40]. The phosphorylated glycoprotein, osteopontin, is also one of the key regulators of bone mineralization and a prevailing inhibitor of vascular calcification [41]. As the MH, bECM/DBM, and PDRN/Span 80 were added to the PLGA composites, these well-known osteogenesis-related markers of expression significantly and gradually increased.

3.4. Biomechanical assessment of fusion mass using three-point bending tests

To measure flexural strength and modulus of the fusion specimens, biomechanical bending tests were performed 8 weeks after material implantation (Fig. 5A–C). Flexural strength is the maximum stress tolerated during compression or tension of a specimen and can be used to evaluate the ability to withstand flexing [42,43]. The results indicated that compared with PLGA implantation, the PME2/PN composite was significantly stronger and broke at a higher strength (Fig. 5D, F). Flexural modulus is measured using the slope of a stress-strain deflection curve and can be used to evaluate the ability to respond to bending forces. Only the PLGA-implanted group had lower flexural modulus values than the autologous bone (Ctrl) group. The other material-implanted groups had overall increased stiffness, the PME2/PN especially had a significantly increased, and the greatest, stiffness (Fig. 5E and F). These results suggested that implantation with PLGA will weaken the strength and, especially, stiffness of fused bone. Co-implantation of MH, ECM/DBM, or PDRN in particular may have an important role.

3.5. Microcomputed tomographic analysis to confirm fusion rate

To confirm bone fusion effects of the materials *in vivo*, bone chips from autologous iliac bone grafts (ABG; Ctrl) were implanted into SD rat PLF models, together with scaffold; lumbar bone was isolated 8 weeks later (Fig. 6A). To identify regenerated bone, segmented bone analysis rather than that of cortical bones using 3D Microcomputed tomographic (micro-CT) analysis of complete reconstructions and cross-sectional cuts was performed (Fig. 6A). All data were analyzed separately for whole bone and new bone; the PME2/PN group had the best performance. The micro-CT results revealed a pattern in which the segmented bones in the group implanted with carrier had a larger increase in bone volume and separation than in the group implanted with autologous bone (Ctrl), but the difference in thickness and number was relatively low. This result indicated that the increase in segmented bone volume implied that the interval between segmented bones increased more by transplantation together with PLGA than with implantation of autologous bone alone. A boosting effect appeared when MH, ECM/DBM, and PDRN were added. As a result, the greatest increase in segmented bone separation occurred when PME2/PN (all carriers included) was implanted. Therefore, the thicknesses of new segmented bone and the entire group of segmented bones were increased (Fig. 6B).

3.6. Histological assessments

Cross sections of fusion sites were analyzed in three ways. Hematoxylin and eosin (H&E) staining showed entire bone areas, including osteoblasts, osteocytes, and osteoclasts, and also inflammatory reactions. Goldner's trichrome (GT) staining showed mineralized bone and osteoid bone area, and Von Kossa (VK) staining showed calcium-positive areas (Fig. 7A).

The bone area (pink-stained area), including osteoblasts (yellow arrow), osteocytes (white arrow), and osteoclasts (white star), was found to be lowest in the Ctrl and PLGA groups and increased in the PM, PME2, and PME2/PN groups. The Ctrl, PLGA, and PME2/PN groups were significantly different. These results indicated that PDRN had an important role in fusion during bone remodeling (Fig. 7A and B). A large number of fibrocartilage chondrocytes (black arrow) were found, which activate angiogenesis by increasing VEGF-A expression after expression of HIF1α under hypoxic conditions [44]. These results indicated that bone fusion was affected by not only osteogenesis but also by angiogenesis.

As a result of confirming the fusion site, the PM, PME2, and PME2/PN groups exhibited more areas of osteoid (orange-red arrow) and mineralization (green arrow), compared with the Ctrl or PLGA groups. The Ctrl, PLGA, and PME2/PN groups were significantly different. These results suggested that PME2/PN boosted mineralization by maturing the unmineralized areas and an organic portion of osteoid (Fig. 7A, C).

This mineralization was also confirmed based on assessment of tissue calcium salts. The lowest values were found in the Ctrl and PLGA groups and were significantly different from the PM, PME2, and PME2/PN groups. The results indicated there was a gradual increase in calcium salt-positive areas (dark brown area; sky blue arrow); the PME2/PN group had the largest value (Fig. 7A, D). These results indicated that PME2/PN had a maturation effect on the fusion site via calcium deposition. All analyses proceeded by randomly selecting sites, excluding the spinal canal and vertebral body containing the spinal cord, and the spinous processes.

3.7. Genetic and molecular assessments to confirm osteogenic differentiation

The increases in bone and in mineralized and Ca^{2+} areas revealed by histological assessment are associated with expression of osteogenesis-related genes and proteins. Therefore, variations in osteogenic markers like collagen type 1 alpha 1 chain (Col1A1), RUNX2, FMOD, osteocalcin, and sclerostin were evaluated.

Col1A1 is the only gene that is not expressed in mature chondrocytes [45]; it is a well-known osteoblastogenesis-related gene. Col1A1 is upregulated during differentiation from immature into mature osteoblasts with ECM capable of expressing ALP [46]. Genetic expression analysis revealed that the Ctrl and PLGA groups had similar expression, but expression sharply increased in PM, especially PME2 and PME2/PN, groups (Fig. 8A). There was no difference in expression levels of PME2 and PME2/PN. This result suggested that PDRN had little effect on Col1A1 expression. In the fusion masses, increased expression of RUNX2 tended to induce differentiation into mature osteoblasts, although gene and protein expression patterns were somewhat inconsistent. The RUNX2 protein expression levels in the PLGA groups decreased more than in all the other groups; PME2 and PME2/PN implants greatly increased RUNX2 expression (Fig. 8B and C). RUNX2 gene expression followed the same trend as protein expression, even if all groups had lower levels than the Ctrl group (Fig. 8A). The PLGA, PM, and PME2 groups had lower FMOD gene expression level than the Ctrl group; only the PME2/PN group was higher and was higher than all other groups (Fig. 8A). Although protein and gene expression patterns were similar, the difference between the Ctrl and PME2/PN group was not significant (Fig. 8B and C). The PLGA, PM, and PME2 groups had lower osteocalcin gene expression than the Ctrl group; the PME2/PN group had the highest expression (Fig. 8A). Protein expression reflected the differences in gene expression. The PLGA group had higher osteocalcin expression than the Ctrl group; the PM, PME2, and PME2/PN groups had sequentially increased osteocalcin expression (Fig. 8B and C). Finally, sclerostin (Sost) acts as an antagonist to prevent excessive bone formation [47]. Sost is usually expressed in osteocytes [48] and also acts to control the matrix mineralization that occurs when immature osteocytes develop into mature osteocytes [49]. Sost gene expression levels were lower in the PLGA, PM, PME2, and PME2/PN groups than in the Ctrl group (Fig. 8A).

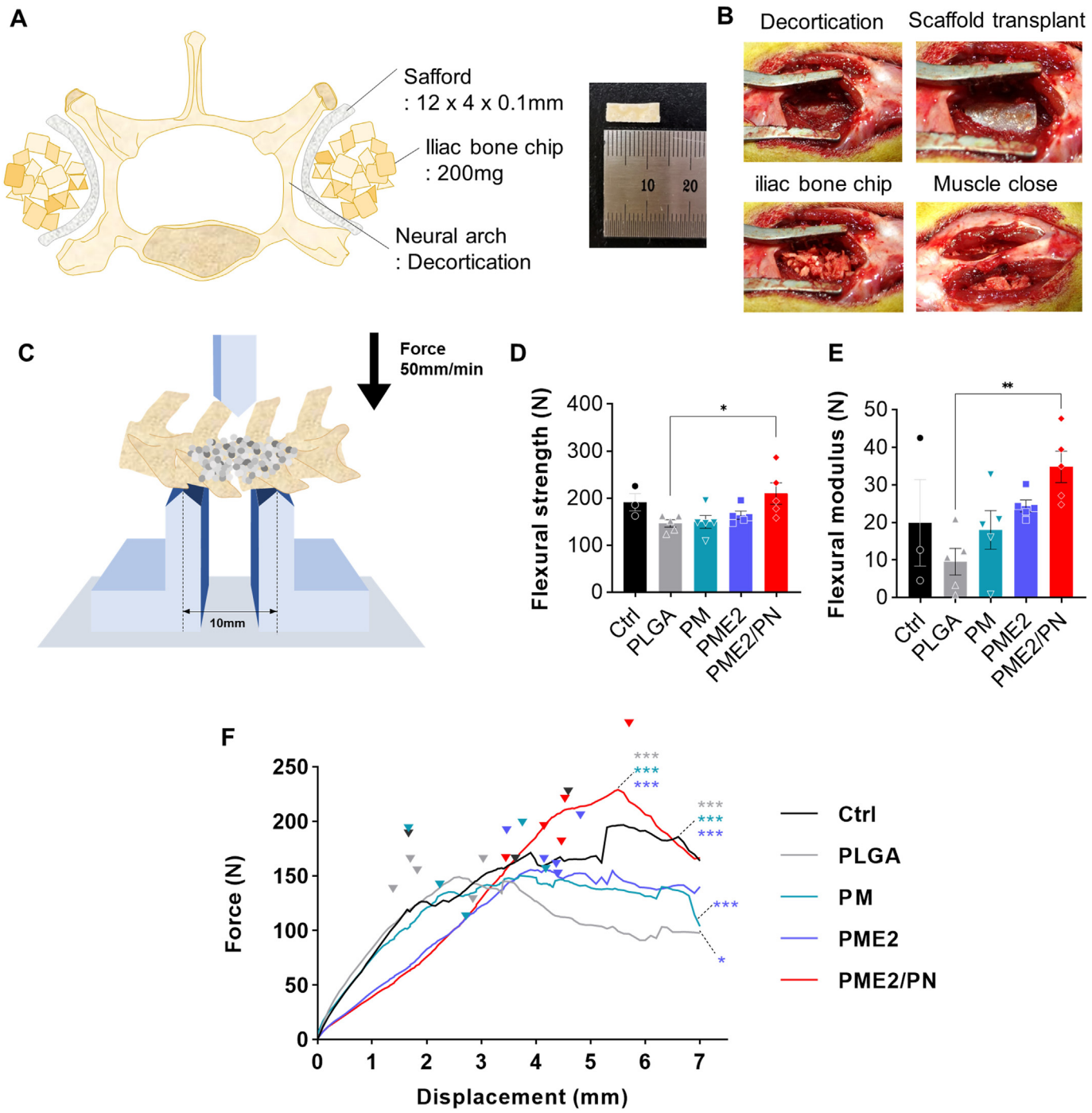

Fig. 5. Scaffold with rat PLF model and biomechanical assessment. (A) Schematic image of rat PLF model. Scaffold and autogenous bone grafting method, position, and implant conditions. (B) Surgical stage of grafting scaffolds and AB to the PLF model. (C) Experimental design for three-point bending test. Arrow indicates direction of force applied to fusion mass. (D) Average ultimate fusion mass breakage strength for each group. (E) Flexural modulus indicates the tension that withstands an applied force. (F) Force-displacement curves of fusion mass for each group and individual flexural strength data. Implantation of PME2/PN increased both flexural strength and flexural modulus at the fusion site. $^{*}p < 0.05$, $^{**}p < 0.01$, and $^{***}p < 0.001$ indicate statistically significant differences.

Sost protein expression levels gradually increased in the PLGA, PM, PME2, and PME2/PN groups than in the Ctrl group, but the differences were not significant (Fig. 8B and C). Increased Sost expression can suppress proliferation and differentiation of osteogenic cells and cause apoptosis [50]. However, bone fusion using PLGA, MH, ECM/DBM, and PDRN/S80 can be accomplished, while activating osteogenesis without excessive bone formation.

Taken together, these results suggested that PLGA did not significantly affect overall osteogenesis and that MH and ECM/DBM had important roles in the expression of Col1A1 and RUNX2 genes important for differentiation of immature osteoblasts; PDRN had little effect at this stage. The results also indicated that PDRN had a crucial role in the maturation and mineralization of osteoblasts. Thus, activating differentiation of undifferentiated cells via activation of various genes associated with osteogenesis revealed the overall mechanism of bone fusion through calcification and mineralization.

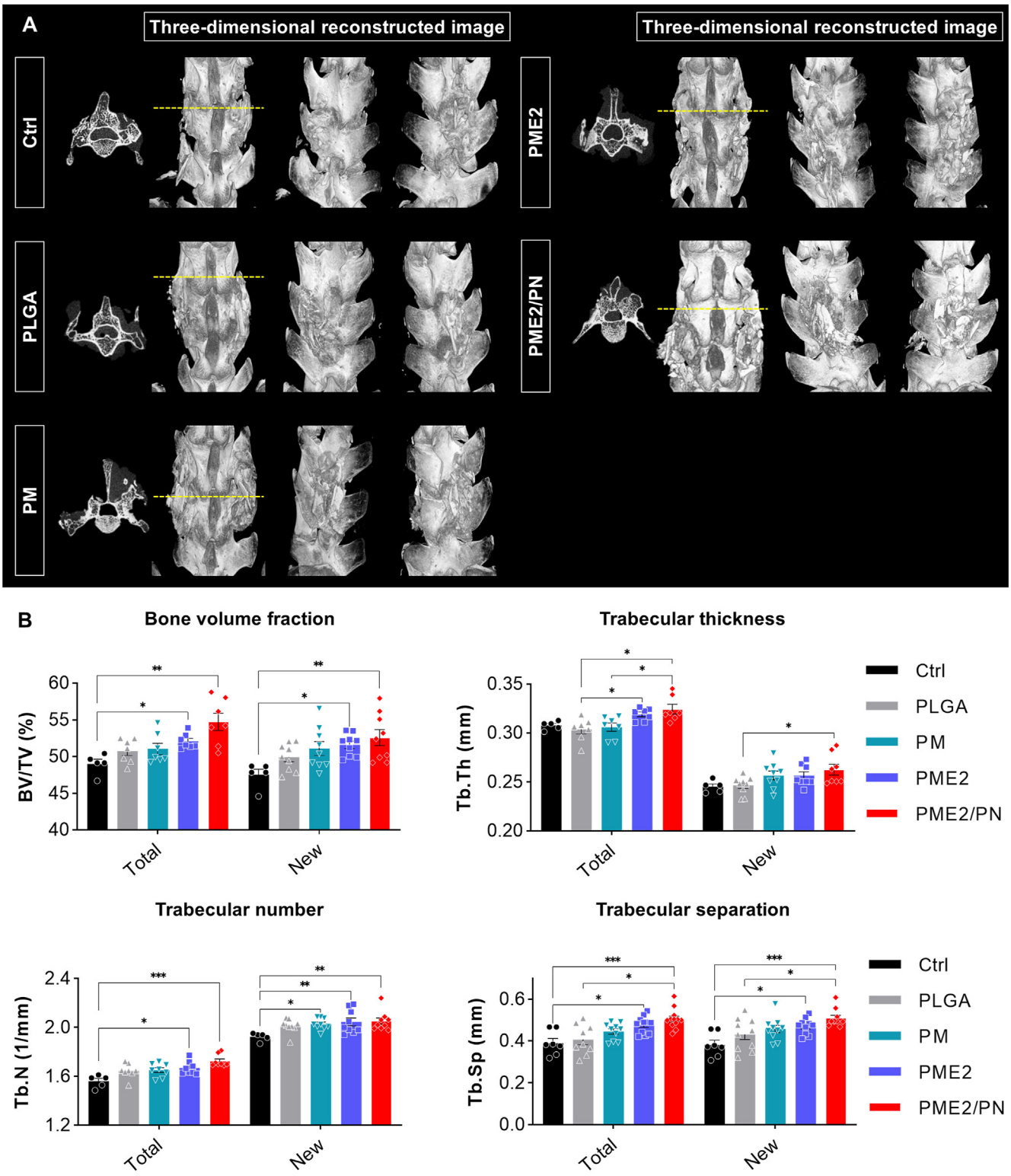

Fig. 6. Microcomputed tomography analysis of total and newly formed bone mass after PLF. (A) 2D and 3D reconstructed micro-CT images of fusion sites. (B) Cancellous bone analysis of total and newly formed bone mass. Implantation of PME2/PN increased the percentage of cancellous bone in both total and newly generated bone. This change appeared as a result of the increased thickness, number, and spacing of cancellous bone. $*p < 0.05$, $**p < 0.01$, and $***p < 0.001$ indicate statistically significant differences.

3.8. Genetic and molecular assessments to confirm angiogenesis

In the case of VEGF-A gene expression, the PM and PME2 groups had significantly higher expression than the Ctrl and PLGA groups; the PME2/PN group was approximately 18 times higher than the Ctrl group (Fig. 9A). VEGF-A-associated protein expression levels were lower in the PLGA, PM, and PME2 than in the Ctrl group; but, the expression level was approximately 1.5 times higher in the PME2/PN group (Fig. 9B and C).

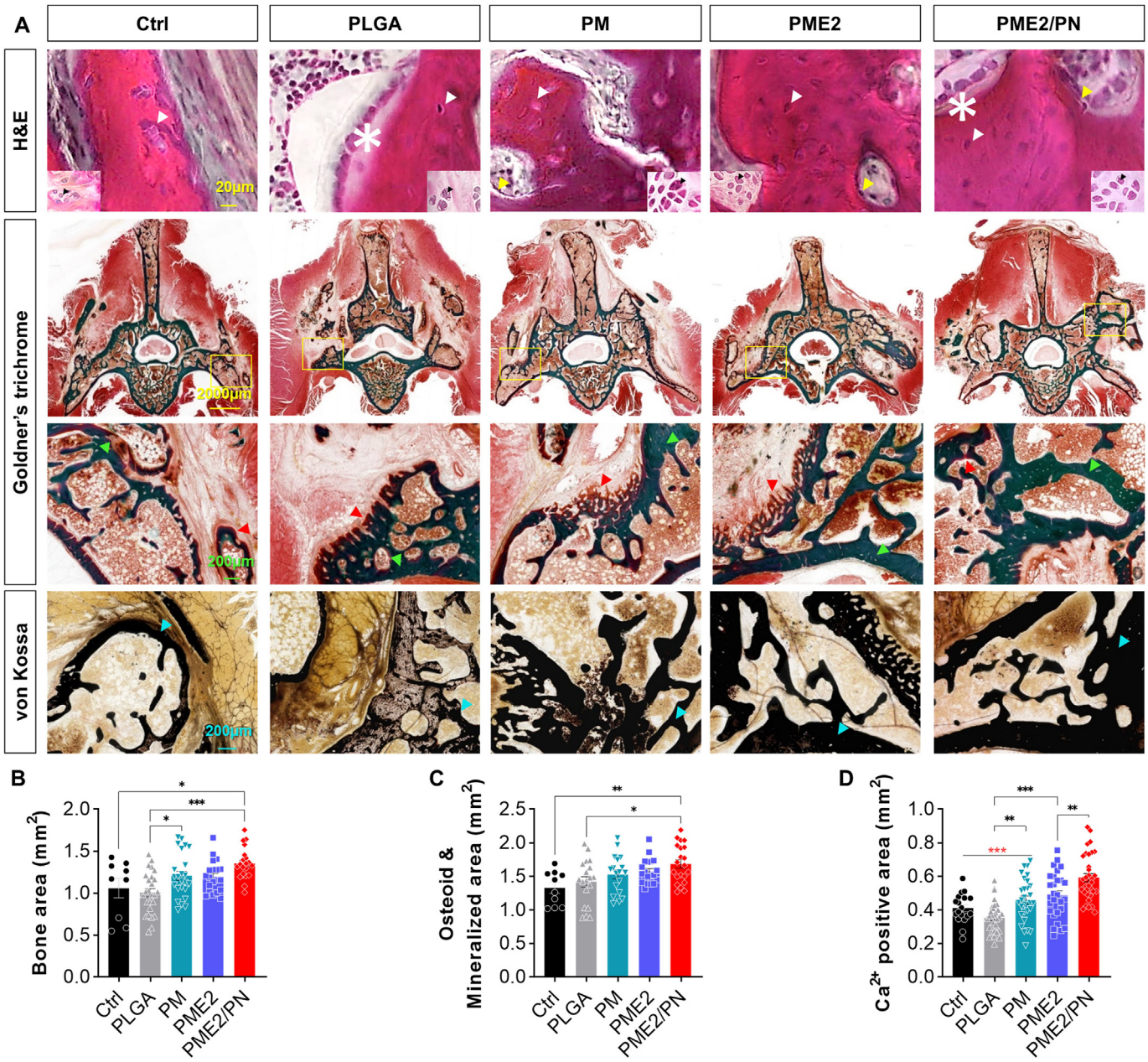

Fig. 7. Histological assessment of fusion mass after PLF. (A) HE stain indicates the inflammatory reaction within the bone area (pink and purple). The bone area contains osteoblasts (yellow arrow), osteocytes (white arrow), and osteoclasts (white star); chondrocytes (small box) were observed in the cartridge area. GT stain indicates osteoid areas (red arrows; red and red) and mineralized areas (light green arrow; blue-green). VK stain indicates Ca^{2+} positive areas (sky blue arrow; dark brown). (B) Graph of bone area, based on HE stain. (C) Graph of osteoid and mineralized areas, based on GT stain. (D) Graph of Ca^{2+} positive area, based on VK stain. Implantation of PME2/PN increased bone areas, osteoid and mineralized areas, and Ca^{2+} positive areas. All images were observed and quantified in spine cross sections. $^{*}p < 0.05$, $^{**}p < 0.01$, and $^{***}p < 0.001$ indicate statistically significant differences.

VEGFR2, a VEGF-A receptor protein, induces migration, proliferation, and survival of endothelial cells (ECs). After it is automatically expressed and secreted by VEGF-producing osteoblasts, regulates the migration, differentiation, and survival of these cells [51]. VEGFR2 gene expression was lower in the PLGA, PM, and PME2 groups than in the Ctrl group; it was approximately 1.2 times higher in the PME2/PN group (Fig. 9A). Protein expression levels were higher in all carrier implant groups than in the Ctrl group; the PME2/PN group had about eight times higher expression (Fig. 9B and C).

Hypoxic conditions that occur during tissue damage and regeneration can activate intracellular signaling pathways through transcriptional regulator hypoxia inducible factor (HIF). HIF can act as a key regulator of VEGF expression and angiogenesis [52]. HIF proteins consist of three α-subunits (HIF1α, HIF2α, and HIF3α) and a β-subunit. Among these subunits, HIF1α has an important role in chondrocyte survival under hypoxic conditions; its expression in osteogenic cells regulates expression of VEGF [53]. The HIF1α gene expression level was higher in all the carrier implant groups than in the Ctrl group; expression was about four times greater in the PM and PME2/PN groups (Fig. 9A).

The glycoprotein, platelet endothelial cell adhesion molecule-1 (CD31), participates in regulation of angiogenesis and angiogenic cell-cell interactions [54]. CD31 is only expressed on ECs, hematopoietic cells, and osteoclasts, but not on osteoblasts [55]. The CD31 gene increased about three times in the PLGA and PM groups, and about eight

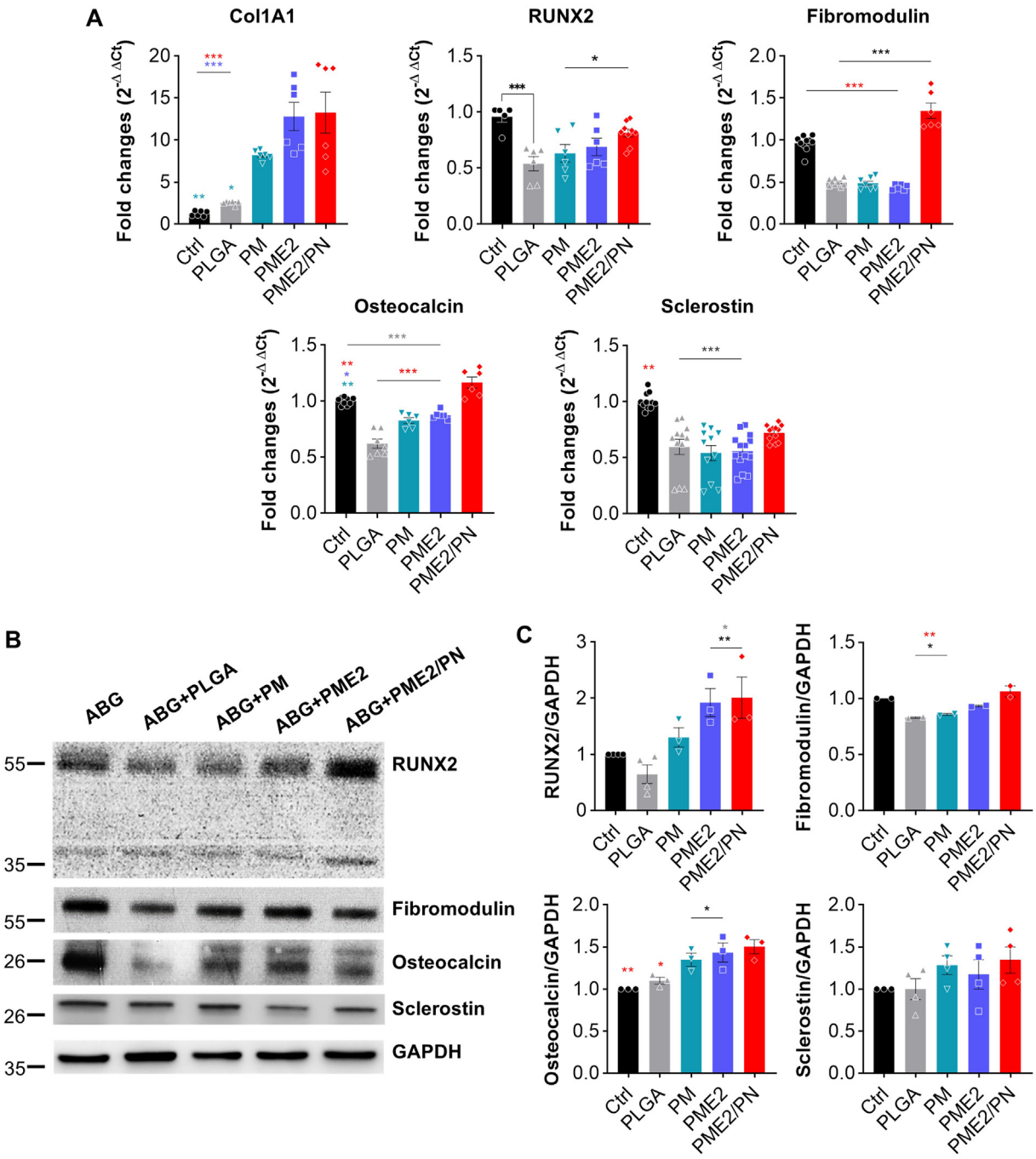

Fig. 8. Genetic and molecular assessment to confirm osteogenesis. (A) Expressions of osteogenic markers, including Col1A1, RUNX2, fibromoduline (FMOD), osteocalcin, and sclerostin (Sost) from fusion mass, qRT-PCR analysis. (B) Western blot (WB) results for RUNX2, FMOD, osteocalcin, and Sost. (C) Expression of RUNX2, FMOD, osteocalcin, and Sost compared with GAPDH, WB analysis. PME2/PN transplantation increased both gene and protein expression of osteogenesis-associated factors. $*p < 0.05$, $**p < 0.01$, and $***p < 0.001$ indicate statistically significant differences.

times in the PME2 and PME2/PN group, compared with the Ctrl group (Fig. 9A). At protein expression levels of CD31, the PLGA, PM, and PME groups were very similar to the Ctrl group; in the PME2/PN group, CD31 protein expression was about 2.5 times greater than in the Ctrl group (Fig. 9B and C).

Compared with the Ctrl group, Ang1 gene expression gradually increased in the PLGA, PM, PME2, and PMEP2/PN groups, in the PMEP2/PN group, Ang1 expression was about 4.5 times higher (Fig. 9A).

The results assume that PLGA did not significantly affect angiogenesis, while MH and ECM/DBM increased angiogenesis in endothelial cells and in osteoblasts. PDRN overwhelmingly increased the expression of all genes related to angiogenesis. To directly affect osteogenesis, some factors are also expressed in osteoclasts and directly or indirectly affect osteogenesis and angiogenesis through osteoclastogenesis. Taken together, these results indicated that during bone fusion, an angiogenesis-related factor was a key participating factor.

3.9. Genetic and molecular assessments to verify anti-inflammatory and macrophage polarization effects in tissue

The presence of iNOS, a macrophage M1 type marker, was confirmed during investigation of anti-inflammatory and macrophage polarization

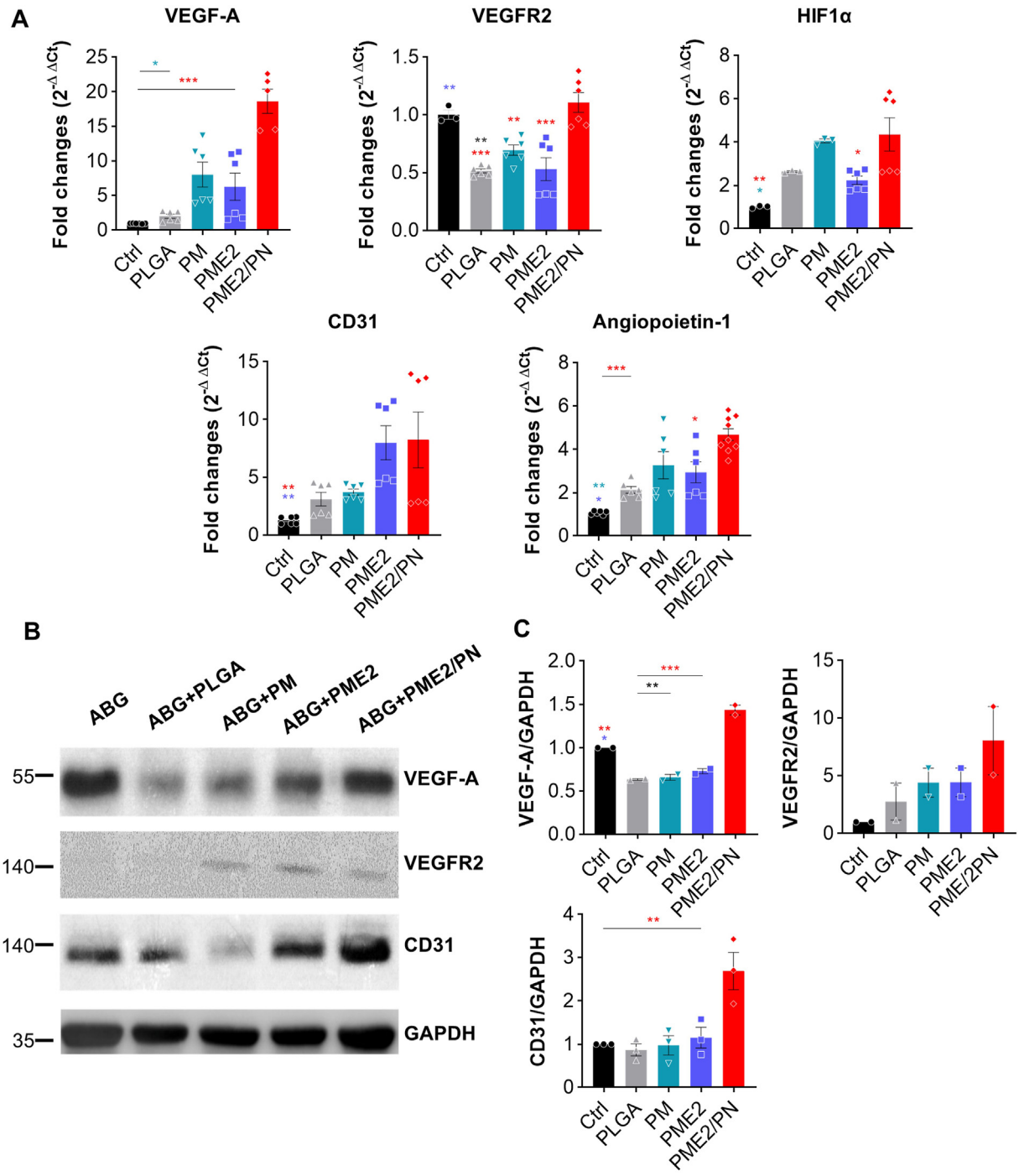

Fig. 9. Genetic and molecular assessment to confirm angiogenesis. (A) Expression of angiogenesis and vascular stabilization markers, including VEGF-A, VEGFR2, HIF1α, CD31, and angiopoietin-1 from fusion mass, qRT-PCR analysis. (B) WB for VEGF-A, VEGFR2, and CD31. (C) Expression of VEGF-A, VEGFR2, and CD31, compared with GAPDH, WB analysis. PME2/PN transplantation significantly enhances gene and protein expression associated with angiogenesis and factors associated with vascular stabilization. $*p < 0.05$, $**p < 0.01$, and $***p < 0.001$ indicate statistically significant differences.

effects *in vivo*. Except for the Ctrl group in which autologous bone was transplanted, expression of M1 greatly increased in all groups. But, in the PMEP2/PN group, the expression level decreased to one-eighth that of the other carrier implant groups (Fig. 10A). In the Ctrl and PLGA groups, CD206 did not change, but it was greatly enhanced (approximately 10–15 times) in the PM and PME2 groups; the PME2/PN group had approximately 30-times higher expression than the Ctrl group (Fig. 10A).

The PLGA, PM, and PME2 groups decreased in TNF-α gene expression more rapidly than the Ctrl group (0.5–0.8 times); it was about 0.35 times more decreased in the PME2/PN group (Fig. 10B). Protein expression increased in the PLGA and PM groups compared with the Ctrl group; expression had a tendency to decrease in the PME2 and PME2/PN groups (Fig. 10C and D). For gene expression, the PLGA group had no anti-inflammatory effect compared with the Ctrl group; PM and PME2 decreased to 0.6–0.8 times and the PME2/PN group decreased about 0.3 times (Fig. 10B). Protein expression was higher than the Ctrl group in all groups; it was about 2.8 times in the PLGA group, 1.8 times in the PM and PME2 groups, and 1.45 times in the PME2/PN group (Fig. 10C and D).

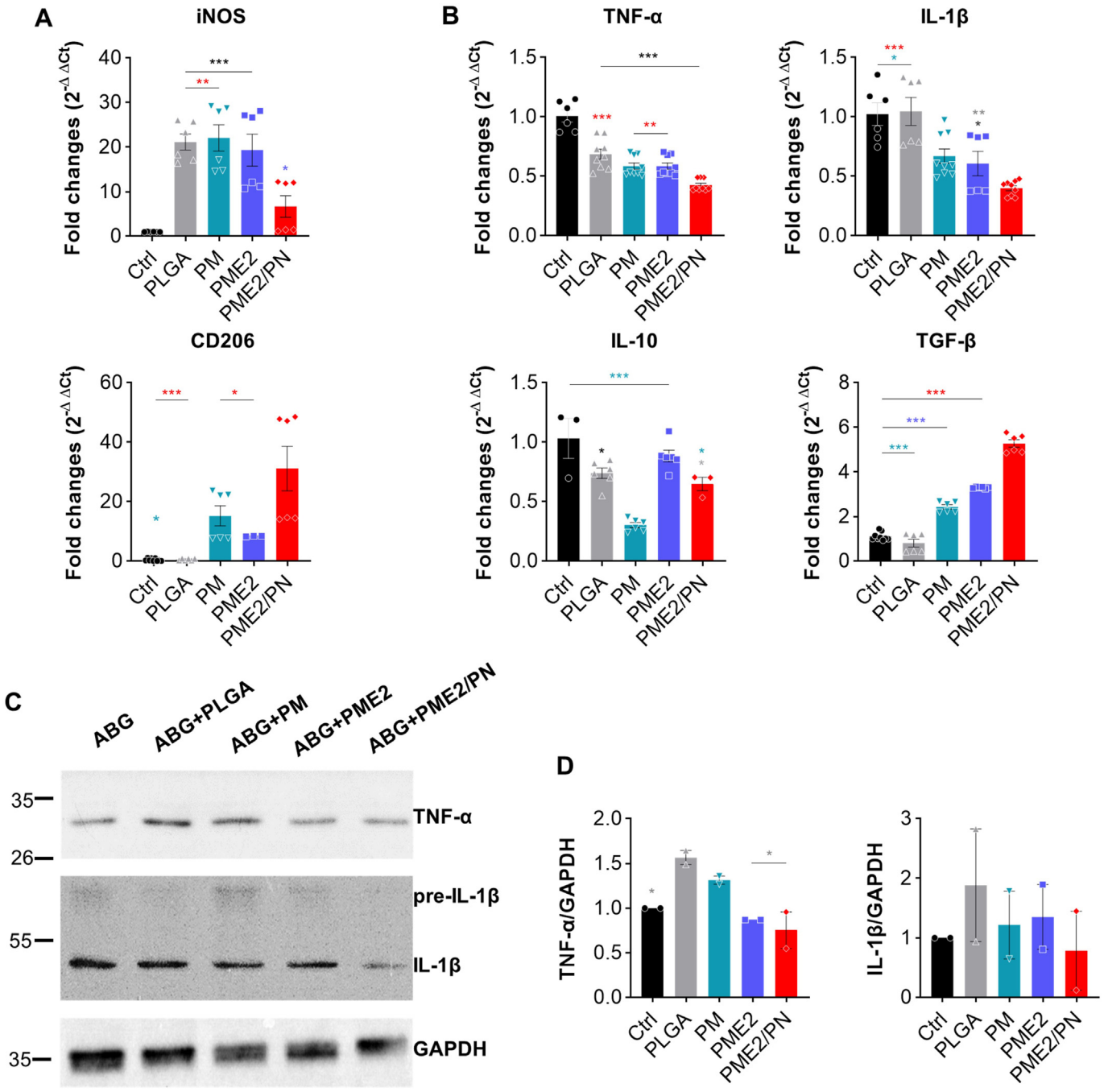

Fig. 10. Genetic and molecular assessment verify immune modulation. (A) Expressions of macrophage and pro- and anti-inflammatory markers, including iNOS, CD206, TNF-α, IL-1β, IL-10, and TGF-β from fusion mass, qRT-PCR analysis. (B) WB for TNF-α and IL-1β. (C) Expression of TNF-α and IL-1β compared with GAPDH, WB analysis. The PME2/PN transplant resulted in polarization to M2-type macrophages that secrete anti-inflammatory cytokines, chemokines, and growth factors. *$p <$ 0.05, **$p < 0.01$, and ***$p < 0.001$ indicate statistically significant differences.

This result can be explained in that IL-1β participates in induction of osteogenic differentiation, as previously described. The cytokine, IL-10, is involved in M2 polarization via oxidative phosphorylation of macrophages [56]. It is secreted by many cells (e.g., lymphocytes, neutrophils, ECs, and mast cells) and affects innate and adaptive immune responses. Overexpressed IL-10 reduces expression of pro-inflammatory mediators, such as IL-6, MCP-1, and heat shock protein 47 [57]. IL-10 expression levels were generally lower in the scaffold-implanted groups than in the Ctrl group. This result can be explained by the amount of IL-10 secreted to induce polarization of macrophages. The expression level of CD206, an M2 marker, was highest in the PME2 group, then sequentially declined in the PM and PME2/PN groups. However, IL-10 not only induces oxidative phosphorylation of macrophages. It is also secreted from M2 at the same time, so the patterns were not identical (Fig. 10B).

The chemokine, TGF-β, has an important role in maintenance of homeostasis in each tissue. Like IL-10, TGF-β is involved in inert, non-antigen-specific, and antigen-specific immune responses [58]. Absence of M1 to M2 conversion during chronic inflammation is characteristic of chronic wounds and can be rescued by injection of exogenous TGF-β [59]. TGF-β was expressed in the PLGA group in the same manner as in the Ctrl group. The expression level gradually increased in the PM and PME2 groups, and the level increased overwhelmingly in the PME2/PN

group. This result can be explained by the presence of a substance secreted from M2 macrophages, unlike IL-10, with similar results as CD206 (Fig. 10B).

Taken together, these results indicated that the carrier had an important role in determination of the macrophage type that regulated the inflammatory environment; the presence or absence of PDRN affects the outcome. Inclusion of PDRN induced polarization into M2-type macrophages that activated angiogenesis and tissue remodeling, resulting in increased secretion of cytokines, chemokines, and growth factors. At the same time, this process resulted in an inhibition of M1 polarization, which led to a decrease in pro-inflammatory cytokines and helped to improve the inflammatory environment and tissue regeneration.

4. Discussion

In this study, we combined an additive for homogenous PDRN dispersion, Span 80, with a nano-emulsion method along with improved bECM/DBM to synthesize a stable scaffold. Controlled release of PDRN from the PLGA composite provides advantages regarding long-term safety and efficacy. Using this strategy, we wanted to examine the properties of the scaffold and the role of each scaffold-constituent material for spine fusion. Each stepwise scaffold was synthesized and then profiled *in vitro* and *in vivo* in various ways. Our analyses provided molecular insights into the variable mechanisms by which substances that made up the scaffold were involved in fusion.

Other studies found that co-administration of inorganic bECM and organic DBM induces BMPs, PDGF, insulin-like growth factors (IGF), FGF, epidermal growth factors (EGF), transforming growth factor or tumor growth factor (TGF), and retinoic acid (RA) [60]. Lee et al. found that a nature-inspired inorganic-organic hydrogel bone sealant has outstanding bone healing ability [61].

Experimental and clinical studies found that BMP effectively induces osteogenic cells when they are combined subcutaneously or implanted together in muscle [62]. BMP-2 and BMP-7 are the most commonly used BMPs in clinical practice; BMP-2 dominates the spine fusion market. As extraction and purification of human BMP from cadaver bones provides only small amounts, production was limited at first [63]. Therefore, gene technology was used to develop rhBMP, which effectively increases bone fusion rates after lumbar surgery and leads to reductions in pseudoarthrosis and iliac bone harvesting. In 2002, the US Food and Drug Administration approved use of rhBMP-2 for anterior lumbar interbody fusion surgery, including one-level degenerative disc disease and spondylolisthesis [11].

Since approval in the USA, BMP has been commonly used off-label as a spine fusion inducer in most kinds of spine fusion surgeries (i.e., in addition to anterior lumbar interbody fusion), including posterior lumbar interbody fusion (PLIF), transforaminal lumbar interbody fusion (TLIF), and cervical or thoracic fusion surgery. However, serious adverse BMP-2-related effects (e.g., infection, osteolysis, ectopic bone formation, retrograde ejaculation, soft tissue edema, and radiculitis) have been reported, and there are concerns about safety issues [63]. This is why a new bone substitute for autologous bone graft or BMP that is both highly effective and stable with safety in all clinical fields is needed.

As previously mentioned, the vascularization property of biomaterials is a crucial concept for bone regeneration. To design an effective biomaterial, we included PDRN in a biomimetic composite because it has excellent pro-angiogenic effects. Most approved forms of PDRN are injectable liquid phases and require other types of processing to introduce them into hard rather than soft tissues, such as leg ulcers, burns, and depressed scars [64,65]. In a previous study, we found that when administered in the body, PDRN selectively exerts anti-inflammatory effects, cell proliferation, and angiogenic effects at injured sites through its adenosine A2a receptor agonistic effect and salvage pathway [19,20]. However, in this study, we found that PDRN affected macrophage polarization via a decrease in M1 and an increase in M2 macrophages. Although it is necessary to continue research on the mechanism via which each of the scaffolding substances that we used affected macrophage polarization, this study revealed immunological aspects of PDRN relevant for tissue engineering approaches. In this work, we investigated a PLGA composite containing a multi-modulated bioactive molecule for spinal fusion. The improved composite (ECM/DBM and PDRN; PME2/PN), which was different from previous studies [19], played an important role in conventional osteogenesis and angiogenesis and macrophage polarization, which are important for tissue recovery. The results showed that PDRN addition induces tissue repair, angiogenesis, and immunosuppression through the secretion of cytokines, chemokines, and growth factors compared to using only ECM. This proof-of-concept study revealed the advantages of advanced biomaterials for bone tissue engineering. Taken together, our results suggest that PME2/PN composite can be a good candidate for improving bone regeneration in spinal fusion surgery.

5. Conclusion

A multi-modulation of the immune-inflammatory response of PME2/PN using bioactive agent incorporation was demonstrated. In both *in vitro* and *in vivo* evaluations, PME2/PN had great biocompatibility and anti-inflammatory effects. Although we primarily focused on the angiogenic ability of PME2/PN, we also meticulously discovered its potential role in induction of macrophage phenotype transition from M1 to M2. This study revealed characteristics of an advanced bone graft material with enhanced anti-inflammatory, angiogenic, osteogenic, and immune modulation activities for bone tissue engineering. These results demonstrate that the PME2/PN composite would be substantially help induce bone formation in spinal fusion surgery.

Credit author statement

Hye Yeong Lee: Conceptualization, Writing – original draft, Validation. **Da-Seul Kim**: Conceptualization, Writing – original draft, Validation. **Gwang Yong Hwang**: Investigation. **Jun-Kyu Lee**: Writing – original draft, Investigation. **Hye-Lan Lee**: Investigation, Data curation, Visualization. **Ji-Won Jung**: Investigation, Data curation, Visualization. **Sae Yeon Hwang**: Investigation, Visualization. **Seung-Woon Baek**: Investigation, Visualization. **Sol lip Yoon**: Investigation. **Yoon Ha**: Investigation. **Keung Nyun Kim**: Investigation. **Inbo Han**: Writing – review & editing. **Dong Keun Han**: Writing – review & editing, Supervision, Funding acquisition. **Chang Kyu Lee**: Writing – review & editing, Supervision, Funding acquisition.

Funding

This study was supported by a faculty research grant of Yonsei University College of Medicine (6-2021-0112), the Basic Science Research Program (2023R1A2C3003807) through the National Research Foundation of Korea, funded by the Ministry of Science and ICT (MSIT), and a grant of the Korea Health Technology R&D Project through the Korea Health Industry Development Institute (KHIDI), funded by the Ministry of Health & Welfare, Republic of Korea (grant number: HI20C0625), Korea Institute for Advancement of Technology (KIAT) grant funded by the Korea Government (MOTIE, grant number: P0015342), and the Korea Medical Device Development Fund grant funded by the Korea government (the Ministry of Science and ICT; the Ministry of Trade, Industry and Energy; the Ministry of Health & Welfare; the Ministry of Food and Drug Safety) (RS-2020-KD000005).

Declaration of competing interest

The authors declare that they have no known competing financial interests or personal relationships that could have appeared to influence the work reported in this paper.

Data availability

Data will be made available on request.

Appendix A. Supplementary data

Supplementary data to this article can be found online at https://doi.org/10.1016/j.mtbio.2023.100611.

References

[1] Y.Z. Jin, G.B. Zheng, M. Cho, J.H. Lee, Effect of Whitlockite as a new bone substitute for bone formation in spinal fusion and ectopic ossification animal model, Biomater. Res. 25 (2021) 34, https://doi.org/10.1186/s40824-021-00237-3.

[2] T. Kang, S.Y. Park, S.H. Hong, J.H. Lee, S.H. Lee, J.H. Park, Bone union after spinal fusion surgery using local bone in long-term bisphosphonate users: a prospective comparative study, Arch. Osteoporosis 14 (2019) 74, https://doi.org/10.1007/s11657-019-0628-8.

[3] J.J. Reid, J.S. Johnson, J.C. Wang, Challenges to bone formation in spinal fusion, J. Biomech. 44 (2011) 213–220, https://doi.org/10.1016/j.jbiomech.2010.10.021.

[4] E. Benzel, L. Ferrara, S. Roy, A. Fleischman, Micromachines in spine surgery, Spine 29 (2004) 601–606, https://doi.org/10.1097/01.brs.0000115141.16396.e6.

[5] C. Li, H.R. Wang, X.L. Li, X.G. Zhou, J. Dong, The relation between zoledronic acid infusion and interbody fusion in patients undergoing transforaminal lumbar interbody fusion surgery, Acta Neurochir. 154 (2012) 731–738, https://doi.org/10.1007/s00701-012-1283-7.

[6] K. Nagahama, M. Kanayama, D. Togawa, T. Hashimoto, A. Minami, Does alendronate disturb the healing process of posterior lumbar interbody fusion? A prospective randomized trial, J. Neurosurg. Spine 14 (2011) 500–507, https://doi.org/10.3171/2010.11.Spine10245.

[7] M.M. Panjabi, Clinical spinal instability and low back pain, J. Electromyogr. Kinesiol. 13 (2003) 371–379, https://doi.org/10.1016/s1050-6411(03)00044-0.

[8] P.C. Reid, S. Morr, M.G. Kaiser, State of the union: a review of lumbar fusion indications and techniques for degenerative spine disease, J. Neurosurg. Spine 31 (2019) 1–14, https://doi.org/10.3171/2019.4.Spine18915.

[9] Y.S. Wang, L. Yin, H. Bao, W.D. Wang, Titanium mesh fusion device in the treatment of thoracolumbar burst fracture, Chin. Med. J. 120 (2007) 246–247.

[10] T.M. Bedair, C.K. Lee, D.S. Kim, S.W. Baek, H.M. Bedair, H.P. Joshi, U.Y. Choi, K.H. Park, W. Park, I. Han, et al., Magnesium hydroxide-incorporated PLGA composite attenuates inflammation and promotes BMP2-induced bone formation in spinal fusion, J. Tissue Eng. 11 (2020), 2041731420967591, https://doi.org/10.1177/2041731420967591.

[11] H.Y. Choi, S.J. Hyun, C.H. Lee, J.H. Youn, M.Y. Ryu, K.J. Kim, Safety and efficacy of recombinant human bone morphogenetic protein-2 in multilevel posterolateral lumbar fusion in a prospective, randomized, controlled trial, Neurospine 19 (2022) 838–846, https://doi.org/10.14245/ns.2244464.232.

[12] C. Frantz, K.M. Stewart, V.M. Weaver, The extracellular matrix at a glance, J. Cell Sci. 123 (2010) 4195–4200, https://doi.org/10.1242/jcs.023820.

[13] H. Lu, T. Hoshiba, N. Kawazoe, I. Koda, M. Song, G. Chen, Cultured cell-derived extracellular matrix scaffolds for tissue engineering, Biomaterials 32 (2011) 9658–9666, https://doi.org/10.1016/j.biomaterials.2011.08.091.

[14] M.S. Birajdar, H. Joo, W.G. Koh, H. Park, Natural bio-based monomers for biomedical applications: a review, Biomater. Res. 25 (2021) 8, https://doi.org/10.1186/s40824-021-00208-8.

[15] M.S. Kang, S.J. Jeong, S.H. Lee, B. Kim, S.W. Hong, J.H. Lee, D.W. Han, Reduced graphene oxide coating enhances osteogenic differentiation of human mesenchymal stem cells on Ti surfaces, Biomater. Res. 25 (2021) 4, https://doi.org/10.1186/s40824-021-00205-x.

[16] L. Polo-Corrales, M. Latorre-Esteves, J.E. Ramirez-Vick, Scaffold design for bone regeneration, J. Nanosci. Nanotechnol. 14 (2014) 15–56, https://doi.org/10.1166/jnn.2014.9127.

[17] V. Karageorgiou, D. Kaplan, Porosity of 3D biomaterial scaffolds and osteogenesis, Biomaterials 26 (2005) 5474–5491, https://doi.org/10.1016/j.biomaterials.2005.02.002.

[18] J.K. Lee, D.S. Kim, S.Y. Park, S.W. Baek, J.W. Jung, T.H. Kim, D.K. Han, Nitric oxide-releasing bioinspired scaffold for exquisite regeneration of osteoporotic bone via regulation of homeostasis, Adv. Sci. (2022), e2205336, https://doi.org/10.1002/advs.202205336.

[19] D.S. Kim, J.K. Lee, J.W. Jung, S.W. Baek, J.H. Kim, Y. Heo, T.H. Kim, D.K. Han, Promotion of bone regeneration using bioinspired PLGA/MH/ECM scaffold combined with bioactive PDRN, Materials 14 (2021), https://doi.org/10.3390/ma14154149.

[20] D.S. Kim, J.K. Lee, J.H. Kim, J. Lee, D.S. Kim, S. An, S.B. Park, T.H. Kim, J.S. Rim, S. Lee, et al., Advanced PLGA hybrid scaffold with a bioactive PDRN/BMP2 nanocomplex for angiogenesis and bone regeneration using human fetal MSCs, Sci. Adv. 7 (2021), eabj1083, https://doi.org/10.1126/sciadv.abj1083.

[21] D. Kim, B. Lee, B. Marshall, S. Thomopoulos, Y.S. Jun, Cyclic strain enhances the early stage mineral nucleation and the modulus of demineralized bone matrix, Biomater. Sci. 9 (2021) 5907–5916, https://doi.org/10.1039/d1bm00884f.

[22] A. Guerrero, A2A adenosine receptor agonists and their potential therapeutic applications. An update, Curr. Med. Chem. 25 (2018) 3597–3612, https://doi.org/10.2174/0929867325666180313110254.

[23] C. Cekic, Y.J. Day, D. Sag, J. Linden, Myeloid expression of adenosine A2A receptor suppresses T and NK cell responses in the solid tumor microenvironment, Cancer Res. 74 (2014) 7250–7259, https://doi.org/10.1158/0008-5472.Can-13-3583.

[24] W. Ji, F. Yang, H. Seyednejad, Z. Chen, W.E. Hennink, J.M. Anderson, J.J. van den Beucken, J.A. Jansen, Biocompatibility and degradation characteristics of PLGA-based electrospun nanofibrous scaffolds with nanoapatite incorporation, Biomaterials 33 (2012) 6604–6614, https://doi.org/10.1016/j.biomaterials.2012.06.018.

[25] B.T. Smith, A. Lu, E. Watson, M. Santoro, A.J. Melchiorri, E.C. Grosfeld, J. van den Beucken, J.A. Jansen, D.W. Scott, J.P. Fisher, et al., Incorporation of fast dissolving glucose porogens and poly(lactic-co-glycolic acid) microparticles within calcium phosphate cements for bone tissue regeneration, Acta Biomater. 78 (2018) 341–350, https://doi.org/10.1016/j.actbio.2018.07.054.

[26] D.S. Kim, J.H. Kim, S.W. Baek, J.K. Lee, S.Y. Park, B. Choi, T.H. Kim, K. Min, D.K. Han, Controlled vitamin D delivery with injectable hyaluronic acid-based hydrogel for restoration of tendinopathy, J. Tissue Eng. 13 (2022), 20417314221122089, https://doi.org/10.1177/20417314221122089.

[27] S.W. Baek, D.H. Song, H.I. Lee, D.S. Kim, Y. Heo, J.H. Kim, C.G. Park, D.K. Han, Poly(L-Lactic acid) composite with surface-modified magnesium hydroxide nanoparticles by biodegradable oligomer for augmented mechanical and biological properties, Materials 14 (2021), https://doi.org/10.3390/ma14195869.

[28] E. Lih, W. Park, K.W. Park, S.Y. Chun, H. Kim, Y.K. Joung, T.G. Kwon, J.A. Hubbell, D.K. Han, A bioinspired scaffold with anti-inflammatory magnesium hydroxide and decellularized extracellular matrix for renal tissue regeneration, ACS Cent. Sci. 5 (2019) 458–467, https://doi.org/10.1021/acscentsci.8b00812.

[29] D.H. Kim, D.S. Kim, H.J. Ha, J.W. Jung, S.W. Baek, S.H. Baek, T.H. Kim, J.C. Lee, E. Hwang, D.K. Han, Fat graft with allograft adipose matrix and magnesium hydroxide-incorporated PLGA microspheres for effective soft tissue reconstruction, Tissue Eng Regen Med 19 (2022) 553–563, https://doi.org/10.1007/s13770-021-00426-0.

[30] E.Y. Shin, D.S. Kim, M.J. Lee, A.R. Lee, S.H. Shim, S.W. Baek, D.K. Han, D.R. Lee, Prevention of chemotherapy-induced premature ovarian insufficiency in mice by scaffold-based local delivery of human embryonic stem cell-derived mesenchymal progenitor cells, Stem Cell Res. Ther. 12 (2021) 431, https://doi.org/10.1186/s13287-021-02479-3.

[31] Y. Miao, Y. Chen, J. Luo, X. Liu, Q. Yang, X. Shi, Y. Wang, Black phosphorus nanosheets-enabled DNA hydrogel integrating 3D-printed scaffold for promoting vascularized bone regeneration, Bioact. Mater. 21 (2023) 97–109, https://doi.org/10.1016/j.bioactmat.2022.08.005.

[32] A. Baek, Y. Kim, J.W. Lee, S.C. Lee, S.R. Cho, Effect of polydeoxyribonucleotide on angiogenesis and wound healing in an in vitro model of osteoarthritis, Cell Transplant. 27 (2018) 1623–1633, https://doi.org/10.1177/0963689718804130.

[33] B. Beamer, C. Hettrich, J. Lane, Vascular endothelial growth factor: an essential component of angiogenesis and fracture healing, HSS J. 6 (2010) 85–94, https://doi.org/10.1007/s11420-009-9129-4.

[34] T. Suzuki, T. Miyamoto, N. Fujita, K. Ninomiya, R. Iwasaki, Y. Toyama, T. Suda, Osteoblast-specific Angiopoietin 1 overexpression increases bone mass, Biochem. Biophys. Res. Commun. 362 (2007) 1019–1025, https://doi.org/10.1016/j.bbrc.2007.08.099.

[35] S. Vimalraj, Alkaline phosphatase: structure, expression and its function in bone mineralization, Gene 754 (2020), 144855, https://doi.org/10.1016/j.gene.2020.144855.

[36] X. Qin, Q. Jiang, T. Miyazaki, T. Komori, Runx2 regulates cranial suture closure by inducing hedgehog, Fgf, Wnt and Pthlh signaling pathway gene expressions in suture mesenchymal cells, Hum. Mol. Genet. 28 (2019) 896–911, https://doi.org/10.1093/hmg/ddy386.

[37] V. Kram, R. Shainer, P. Jani, J.A.N. Meester, B. Loeys, M.F. Young, Biglycan in the skeleton, J. Histochem. Cytochem. 68 (2020) 747–762, https://doi.org/10.1369/0022155420937371.

[38] M. Brunner, A. Millon-Frémillon, G. Chevalier, I.A. Nakchbandi, D. Mosher, M.R. Block, C. Albigès-Rizo, D. Bouvard, Osteoblast mineralization requires beta1 integrin/ICAP-1-dependent fibronectin deposition, J. Cell Biol. 194 (2011) 307–322, https://doi.org/10.1083/jcb.201007108.

[39] G. Wolf, Function of the bone protein osteocalcin: definitive evidence, Nutr. Rev. 54 (1996) 332–333, https://doi.org/10.1111/j.1753-4887.1996.tb03798.x.

[40] R. Fujisawa, M. Tamura, Acidic bone matrix proteins and their roles in calcification, Front Biosci (Landmark Ed) 17 (2012) 1891–1903, https://doi.org/10.2741/4026.

[41] S.A. Lund, C.M. Giachelli, M. Scatena, The role of osteopontin in inflammatory processes, J Cell Commun Signal 3 (2009) 311–322, https://doi.org/10.1007/s12079-009-0068-0.

[42] P.A. Guertin, Adaptations of the motor system in animal models of spinal cord injury and disuse, in: Biomechanics in Applications, IntechOpen, 2011.

[43] B. Kamal, D. Russell, A. Payne, D. Constante, K.E. Tanner, H. Isaksson, N. Mathavan, S.R. Cobb, Biomechanical properties of bone in a mouse model of Rett syndrome, Bone 71 (2015) 106–114.

[44] E. Schipani, C. Maes, G. Carmeliet, G.L. Semenza, Regulation of osteogenesis-angiogenesis coupling by HIFs and VEGF, J. Bone Miner. Res. 24 (2009) 1347–1353, https://doi.org/10.1359/jbmr.090602.

[45] P. Gómez-Picos, B.F. Eames, On the evolutionary relationship between chondrocytes and osteoblasts, Front. Genet. 6 (2015) 297, https://doi.org/10.3389/fgene.2015.00297.

[46] S. Kannan, J. Ghosh, S.K. Dhara, Osteogenic differentiation potential of porcine bone marrow mesenchymal stem cell subpopulations selected in different basal media, Biol Open 9 (2020), https://doi.org/10.1242/bio.053280.

[47] A.G. Robling, P.J. Niziolek, L.A. Baldridge, K.W. Condon, M.R. Allen, I. Alam, S.M. Mantila, J. Gluhak-Heinrich, T.M. Bellido, S.E. Harris, et al., Mechanical

stimulation of bone in vivo reduces osteocyte expression of Sost/sclerostin, J. Biol. Chem. 283 (2008) 5866–5875, https://doi.org/10.1074/jbc.M705092200.
[48] L.F. Bonewald, The amazing osteocyte, J. Bone Miner. Res. 26 (2011) 229–238, https://doi.org/10.1002/jbmr.320.
[49] G.J. Atkins, P.S. Rowe, H.P. Lim, K.J. Welldon, R. Ormsby, A.R. Wijenayaka, L. Zelenchuk, A. Evdokiou, D.M. Findlay, Sclerostin is a locally acting regulator of late-osteoblast/preosteocyte differentiation and regulates mineralization through a MEPE-ASARM-dependent mechanism, J. Bone Miner. Res. 26 (2011) 1425–1436, https://doi.org/10.1002/jbmr.345.
[50] A. Chandra, T. Lin, T. Young, W. Tong, X. Ma, W.J. Tseng, I. Kramer, M. Kneissel, M.A. Levine, Y. Zhang, et al., Suppression of sclerostin alleviates radiation-induced bone loss by protecting bone-forming cells and their progenitors through distinct mechanisms, J. Bone Miner. Res. 32 (2017) 360–372, https://doi.org/10.1002/jbmr.2996.
[51] X. Duan, Y. Murata, Y. Liu, C. Nicolae, B.R. Olsen, A.D. Berendsen, Vegfa regulates perichondrial vascularity and osteoblast differentiation in bone development, Development 142 (2015) 1984–1991, https://doi.org/10.1242/dev.117952.
[52] J. Aragonés, P. Fraisl, M. Baes, P. Carmeliet, Oxygen sensors at the crossroad of metabolism, Cell Metabol. 9 (2009) 11–22, https://doi.org/10.1016/j.cmet.2008.10.001.
[53] Y. Wang, C. Wan, L. Deng, X. Liu, X. Cao, S.R. Gilbert, M.L. Bouxsein, M.C. Faugere, R.E. Guldberg, L.C. Gerstenfeld, et al., The hypoxia-inducible factor alpha pathway couples angiogenesis to osteogenesis during skeletal development, J. Clin. Invest. 117 (2007) 1616–1626, https://doi.org/10.1172/jci31581.
[54] N. Ilan, J.A. Madri, PECAM-1: old friend, new partners, Curr. Opin. Cell Biol. 15 (2003) 515–524, https://doi.org/10.1016/s0955-0674(03)00100-5.
[55] Y. Wu, K. Tworkoski, M. Michaud, J.A. Madri, Bone marrow monocyte PECAM-1 deficiency elicits increased osteoclastogenesis resulting in trabecular bone loss, J. Immunol. 182 (2009) 2672–2679, https://doi.org/10.4049/jimmunol.0802398.
[56] R.L. Lopes, T.J. Borges, R.F. Zanin, C. Bonorino, IL-10 is required for polarization of macrophages to M2-like phenotype by mycobacterial DnaK (heat shock protein 70), Cytokine 85 (2016) 123–129, https://doi.org/10.1016/j.cyto.2016.06.018.
[57] W.H. Peranteau, L. Zhang, N. Muvarak, A.T. Badillo, A. Radu, P.W. Zoltick, K.W. Liechty, IL-10 overexpression decreases inflammatory mediators and promotes regenerative healing in an adult model of scar formation, J. Invest. Dermatol. 128 (2008) 1852–1860, https://doi.org/10.1038/sj.jid.5701232.
[58] L. Yang, Y. Pang, H.L. Moses, TGF-beta and immune cells: an important regulatory axis in the tumor microenvironment and progression, Trends Immunol. 31 (2010) 220–227, https://doi.org/10.1016/j.it.2010.04.002.
[59] S. Okizaki, Y. Ito, K. Hosono, K. Oba, H. Ohkubo, H. Amano, M. Shichiri, M. Majima, Suppressed recruitment of alternatively activated macrophages reduces TGF-β1 and impairs wound healing in streptozotocin-induced diabetic mice, Biomed. Pharmacother. 70 (2015) 317–325, https://doi.org/10.1016/j.biopha.2014.10.020.
[60] R. Zhao, R. Yang, P.R. Cooper, Z. Khurshid, A. Shavandi, J. Ratnayake, Bone grafts and substitutes in dentistry: a review of current trends and developments, Molecules 26 (2021), https://doi.org/10.3390/molecules26103007.
[61] C.S. Lee, H.S. Hwang, S. Kim, J. Fan, T. Aghaloo, M. Lee, Inspired by nature: facile design of nanoclay-organic hydrogel bone sealant with multifunctional properties for robust bone regeneration, Adv. Funct. Mater. 30 (2020), https://doi.org/10.1002/adfm.202003717.
[62] M. Cha, Y.Z. Jin, J.W. Park, K.M. Lee, S.H. Han, B.S. Choi, J.H. Lee, Three-dimensional printed polylactic acid scaffold integrated with BMP-2 laden hydrogel for precise bone regeneration, Biomater. Res. 25 (2021) 35, https://doi.org/10.1186/s40824-021-00233-7.
[63] A. Faundez, C. Tournier, M. Garcia, S. Aunoble, J.C. Le Huec, Bone morphogenetic protein use in spine surgery-complications and outcomes: a systematic review, Int. Orthop. 40 (2016) 1309–1319, https://doi.org/10.1007/s00264-016-3149-8.
[64] P. Rubegni, G. De Aloe, C. Mazzatenta, L. Cattarini, M. Fimiani, Clinical evaluation of the trophic effect of polydeoxyribonucleotide (PDRN) in patients undergoing skin explants. A Pilot Study, Curr. Med. Res. Opin. 17 (2001) 128–131.
[65] J.H. Kim, T.R. Kwon, S.E. Lee, Y.N. Jang, H.S. Han, S.K. Mun, B.J. Kim, Comparative evaluation of the effectiveness of novel hyaluronic acid-polynucleotide complex dermal filler, Sci. Rep. 10 (2020) 5127, https://doi.org/10.1038/s41598-020-61952-w.